Composite Structures 389 (2026) 120313

Contents lists available at ScienceDirect

Composite Structures

journal homepage: www.elsevier.com/locate/compstruct

Modeling the influence of anchor spikes on the bond behavior of FRCM applied to curved masonry substrates

Natalia Pingaro [a,b,*], Gabriele Milani [a], Mario Fagone [c], Tommaso Rotunno [d], Ernesto Grande [e,f]

[a] Department of Architecture, Built Environment and Construction Engineering (ABC), Politecnico di Milano, piazza Leonardo da Vinci 32, 20133 Milan, Italy
[b] European Centre for Training and Research in Earthquake Engineering, Eucentre, via Adolfo Ferrata 1, 27100 Pavia, Italy
[c] Department of Civil and Environmental Engineering, University of Florence, via di S. Marta 3, 50139 Florence, Italy
[d] Department of Architecture, University of Florence, Piazza F. Brunelleschi 6, 50121 Florence, Italy
[e] Department of Civil and Mechanical Engineering, University of Cassino and Southern Lazio, via G. Di Biasio 43 03043, Cassino (FR), Italy
[f] European University of Technology EUt+, European Union, Italy

ARTICLE INFO

Keywords:
FRCM
Curved stack bond masonry prisms
Spike anchor
Shear-lap test
Simplified numerical model
Explicit numerical solution (RK4)

ABSTRACT

A phenomenological numerical model for the prediction of the bond behavior of Fiber Reinforced Cementitious Matrix (FRCM) strengthened curved stack bond masonry prisms subjected to single lap shear tests, additionally equipped with spike anchors, is presented. The model lumps all non-linearity in a zero-thickness interface layer between reinforcement, assumed elastic, and curved substrate, supposed rigid. Furthermore, anchor spikes are modeled by means of a linear spring connecting the reinforcement layer located on the free edge side with that positioned between the spike and the loaded edge. A standard second-order non-linear differential equation is derived to describe the mechanical behavior. Numerically, the problem is tackled explicitly, making use of a standard Runge-Kutta in-house developed kernel where the boundary condition at the loaded edge is transferred to the free one. Comparisons with a wide experimental program carried out by the authors on laboratory-scaled curve masonry prisms assembled from stacked units and mortar layers, reinforced with FRCM and equipped with a central spike confirm the predictive capabilities of the simple model proposed, underscoring (i) the role played by curvature in modulating the post-peak response, with an enhanced relative energy dissipation gain in the presence of spike anchors despite an overall reduction with increasing curvature, and (ii) the very moderate effect in terms of peak strength improvement. This post-peak enhancement should therefore be interpreted as a conditional benefit associated with the presence of the spike anchor, contrasting the detrimental role played by curvature.

1. Introduction

Fiber Reinforced Cementitious Matrix (FRCM) [1,2] strengthening systems are nowadays considered a standard approach for the repair and upgrading of masonry structures [1,3]. Further applications can be found for masonry walls [4,5] and arches [6], while several studies extend the analysis to dynamic loading conditions [7,8] or investigate alternative technologies, such as steel reinforced grout (SRG) systems consisting of steel cords embedded within a cementitious matrix [9].

The widespread use of FRCM systems is mainly motivated by rapid installation, reversibility, good vapor permeability, and corrosion resistance. They are commonly applied as external strips, providing moderate strength and ductility enhancement with low invasiveness and easy removability. In historic masonry constructions, such systems are frequently used on arches and vaults [10,11], making applications on curved substrates common. When installed at the intrados, curvature induces positive (detachment) normal stresses at the reinforcement–matrix interface, which may be detrimental to bond strength and reduce the effectiveness of the strengthening system.

To evaluate the basic features of such reinforcing systems, particular attention has been devoted to their debonding behavior [12–14]. Further experimental and analytical investigations are reported in [15–17]. As far as experimentation is concerned, it is hard to measure the debonding evolution in FRCM systems locally. Digital image correlation (DIC) proved to be powerful for Fiber Reinforced Polymer (FRP) [18] strengthened panels, but it is not much of help for FRCMs because strains are measured on the external matrix layer. On the other hand,

* Corresponding author at: Department of Architecture, Built Environment and Construction Engineering (ABC), Politecnico di Milano, piazza Leonardo da Vinci 32, 20133 Milan, Italy.
E-mail address: natalia.pingaro@polimi.it (N. Pingaro).

https://doi.org/10.1016/j.compstruct.2026.120313
Received 27 October 2025; Received in revised form 28 March 2026; Accepted 31 March 2026
Available online 4 April 2026

Nomenclature

BVP	Boundary Value Problem
B_F	Reinforcement's width
CAI	Curvature bonded surface $1/1500\ \text{mm}^{-1}$
CBI	Curvature bonded surface $1/3000\ \text{mm}^{-1}$
C_1^I	Constant of integration, debonding differential equation, interface in stage I
C_1^{II}	Constant of integration, debonding differential equation, interface in stage II
C_1^{III}	Constant of integration, debonding differential equation, interface in stage III
C_2^I	Constant of integration, debonding differential equation, interface in stage I
C_2^{II}	Constant of integration, debonding differential equation, interface in stage II
C_2^{III}	Constant of integration, debonding differential equation, interface in stage III
DIC	Digital Image Correlation
E_F	Reinforcement's elastic modulus
FRCM	Fiber Reinforced Cementitious Matrix
FRP	Fiber Reinforced Polymer
F_L	Force applied at the loaded edge ($F_L = \sigma_F(L_b)E_F t_F$)
F_e	Force applied at the elastic limit, global $U_{F,L}$-F_L curve
F_{max}	Maximum force applied, global $U_{F,L}$-F_L curve
I, II, III	Stages of the trilinear interface constitutive law
IVP	Initial Value Problem
K_1	Equivalent elastic stiffness, global $U_{F,L}$-F_L curve
K_I	Interface in stage I, elastic stiffness ($K_I = \frac{\tau_{L,0M}}{s_{L,0e}}$)
K_s	Spike stiffness (N/mm^3) normalized against reinforcement cross-section area
$K_s{}'$	Spike hardening stiffness (N/mm^3) normalized against reinforcement cross-section area
K_{sp}	Spike spring stiffness (N/mm), $K_{sp} = K_s E_F t_F$
L	Portion of the bonded length between the spike and the free edge
L_b	Bonded length
R	Portion of the bonded length between spike and loaded edge
R_c	Curvature radius of the bonded surface
$U_{F,L}$	Displacement/slip at the loaded edge
$U_{F,L,e}$	Loaded edge displacement at the elastic limit, global $U_{F,L}$-F_L curve
$U_{F,L,u}$	Loaded ultimate displacement, global $U_{F,L}$-F_L curve
$U_F(x)$	Fiber layer's displacement
$U_{s,e}$	Spike elongation at the elastic limit (mm)
$U_{s,u}$	Spike ultimate elongation (mm)
$U_s(\sigma_{F,s})$	Spike elongation when acting stress is equal to $\sigma_{F,s}$
W/O AS	WithOut Anchor Spike
WAS	With Anchor Spike
$f_{t,s}$	Stress at the elastic limit in the axial spring representing the spike
h	Runge-Kutta algorithm and finite difference method, step size discretization of one half of the bonded length ($L_b/2$)
k	time step (k-th slip increment applied at the loaded edge)
$n+1$	Runge-Kutta algorithm and finite difference method, total number of knot points in one half of the bonded length ($n = L_b/2h$)
n_I	Wildcard, n_I=I, II, III
$s, s(x)$	Local slip
s_{II}^s	Slip in correspondence of the spike $s_{II}^s = s_{II}\left(\frac{L_b}{2}\right)$, stage II
$s_{L,0e}$	Interface slip at $\tau_{L,0M}$
$s_{L,0u}$	Interface slip at $\tau_{L,0r}$
$s_{L,se}$	Interface slip at $\tau_{L,sM}$, L part
$s_{L,su}$	Interface slip at $\tau_{L,sr}$, L part
$s_{R,0e}$	Interface slip at $\tau_{R,0M}$
$s_{R,0u}$	Interface slip at $\tau_{R,0r}$
$s_{R,se}$	Interface slip at $\tau_{R,sM}$, R part
$s_{R,su}$	Interface slip at $\tau_{R,sr}$, R part
$\bar{s}_0$	Slip applied at the free edge (Runge-Kutta numerical approach)
$\bar{s}_{I0}$	Slip applied at the free edge, assuming the L left part interface in stage I
$s_I, s_I(x)$	Slip for an interface in stage I
$s_{II}, s_{II}(x)$	Slip for an interface in stage II
$s_{III}, s_{III}(x)$	Slip for an interface in stage III
t_F	Reinforcement's thickness
x	One-dimensional coordinate along the bonded length (origin located at the free edge)
$x_{II,III}$	Abscissa ($L_b/2 < x_{II,III} \leq L_b$) where the interface passes from stage II to stage III
y_1	Slip, L part (s_L) and R part (s_R)
y_1^i	Finite difference method, value of y_1 at the i-th knot point
y_2	First derivative of the slip, L part (s_L') and R part (s_R')
y_2^i	Finite difference method, value of y_2 at the i-th knot point
$\boldsymbol{f}(\boldsymbol{y})$	Runge-Kutta algorithm, $\boldsymbol{f}(\boldsymbol{y}) = [\,\tau(y_1)/E_F t_F \quad y_2\,]^T$
$\boldsymbol{k}_1$	Runge-Kutta algorithm, $\boldsymbol{k}_1 = h\boldsymbol{f}(\boldsymbol{y}_i, x_i)$
$\boldsymbol{k}_2$	Runge-Kutta algorithm, $\boldsymbol{k}_2 = h\boldsymbol{f}\left(\boldsymbol{y}_i + \frac{\boldsymbol{k}_1}{2}, x_i + \frac{h}{2}\right)$
$\boldsymbol{k}_3$	Runge-Kutta algorithm, $\boldsymbol{k}_3 = h\boldsymbol{f}\left(\boldsymbol{y}_i + \frac{\boldsymbol{k}_2}{2}, x_i + \frac{h}{2}\right)$
$\boldsymbol{k}_4$	Runge-Kutta algorithm, $\boldsymbol{k}_4 = h\boldsymbol{f}(\boldsymbol{y}_i + \boldsymbol{k}_3, x_i + h)$
$\boldsymbol{y}$	Dependent variable vector in the Runge-Kutta algorithm, $\boldsymbol{y} = [\,y_1 \quad y_2\,]^T$
$\boldsymbol{y}_i$	Runge-Kutta algorithm, solution vector at knot point $x_i = (i-1)h(i = 1, \cdots, n+1)$ and $x_i = (i-1)h + L_b/2(i = 1, \cdots, n+1)$
α	Interface in stage I, constant ($\alpha = \sqrt{\frac{K_I}{E_F t_F}}$)
$\alpha^{n_I,k-1}$	Slope of the $\tau - s$ piecewise linear interface constitutive law, stage n_I, time step $k-1$
β	Interface in stage II, constant ($\beta = \sqrt{\frac{1}{E_F t_F}\frac{\tau_{R,0M} - \tau_{R,0r}}{s_{R,0u} - s_{R,0e}}}$)
$\beta^{n_I,k-1}$	Y-intercept of the $\tau - s$ piecewise linear interface constitutive law, stage n_I, time step $k-1$
γ	Interface in stage II, constant ($\gamma = \frac{1}{E_F t_F}\frac{\tau_{R,0M}s_{R,0u} - \tau_{R,0r}s_{R,0e}}{s_{R,0u} - s_{R,0e}}$)
$\eta_{L,0}$	Coefficient (non-dimensional) equal to $s_{L,0u}/s_{L,0e} - 1 > 0$, L part
$\eta_{L,s}$	Coefficient (non-dimensional) equal to $s_{L,su}/s_{L,se} - 1 > 0$, L part
$\eta_{R,0}$	Coefficient (non-dimensional) equal to $s_{R,0u}/s_{R,0e} - 1 > 0$, R part
$\eta_{R,s}$	Coefficient (non-dimensional) equal to $s_{R,su}/s_{R,se} - 1 > 0$, R part
$\mu_{L,M}$	Friction coefficient at peak for the L part
$\mu_{L,r}$	Residual friction coefficient for $\sigma_n < 0$, L part
$\mu_{R,M}$	Friction coefficient at peak for the R part
$\mu_{R,r}$	Residual friction coefficient for $\sigma_n < 0$, R part
μ_k	Pre-peak ductility ($\mu_k = U_{Fmax,L}/U_{F,L,e}$), global $U_{F,L}$-F_L curve
$\rho_{L,r}$	Coefficient (dimension [1/MPa]) simulating the observed residual resistance drop for $\sigma_n > 0$, L part
$\rho_{L,\eta}$	Coefficient (non-dimensional) which rules the ratio $\eta_{L,0}/\eta_{L,s}$ with $\sigma_n > 0$ and equal to $1/\sigma_n(\ln\eta_{L,0} - \ln\eta_{L,s})$, L part

$\rho_{R,r}$	Coefficient (dimension [1/MPa]) simulating the observed residual resistance drop for $\sigma_n > 0$, R part
$\rho_{R,\eta}$	Coefficient (non-dimensional) which rules the ratio $\eta_{R,0}/\eta_{R,s}$ with $\sigma_n > 0$ and equal to $1/\sigma_n(\ln\eta_{R,0} - \ln\eta_{R,s})$, L part
$\sigma_F, \sigma_F(x)$	Reinforcement tensile stress
σ_F^s	Reinforcement normal stress in correspondence with the spike
$\sigma_{F,s}$	Spike stress in stage II when the spike constitutive behavior is considered trilinear with softening
$\tau, \tau(x)$	Reinforcement-support interface tangential stress
$\tau - s, \tau(s)$	Constitutive behavior of the reinforcement-support interface
$\tau_{L,0M}$	Peak tangential strength for L interface with $\sigma_n = 0$
$\tau_{L,0r}$	Residual tangential strength for L interface with $\sigma_n = 0$
$\tau_{L,sM}$	Peak tangential strength for L interface with $\sigma_n \neq 0$
$\tau_{L,sr}$	Residual tangential strength for L interface with $\sigma_n \neq 0$
$\tau_{R,0M}$	Peak tangential strength for R interface with $\sigma_n = 0$
$\tau_{R,0r}$	Residual tangential strength for R interface with $\sigma_n = 0$
$\tau_{R,sM}$	Peak tangential strength for R interface with $\sigma_n \neq 0$
$\tau_{R,sr}$	Residual tangential strength for R interface with $\sigma_n \neq 0$

optic fibers tend to introduce a perturbation within the fiber net, are expensive, and difficult to install [15].

In debonding tests, the specimens are typically stacked bond prisms, then externally reinforced with an FRCM strip, which is longitudinally pulled at one edge. Several numerical models have been proposed for the simulation of single-lap shear tests on FRCM-reinforced masonry specimens, often based on interface-based formulations [19–21]. Multilayer and finite element approaches have also been explored [22–25], together with further extensions reported in the literature [26–29].

Despite the importance of the matter, only a limited number of experimental [30–32] and numerical [33–39] studies are available, shedding light on the bond behavior of FRCM when applied to curved masonry supports. These contributions generally confirm that the application at the intrados -albeit very diffused because more practical- is mechanically not the best option, being associated with premature debonding. To counteract such detrimental effects, taking inspiration from the technology used for FRP [40–42], anchor spikes may be introduced to delay debonding in curved masonry elements, especially in cases where the reinforcement is applied at the intrados.

The topic is much more specific than the curved case in the absence of spikes, and the literature is proportionally smaller. Even from an experimental point of view, it is possible to refer to a few works, e.g. [43–46], whereas the available numerical literature on FRCM systems equipped with spike anchors is still limited and mainly oriented toward finite element or phenomenological approaches, often without an explicit low-dimensional formulation capable of interpreting the two-stage bond response, particularly in the presence of curvature-induced normal stresses. Different from FRP, the information gathered from [44] in the case of FRCM indicates that spikes' efficacy is very moderate. A little effect on the improvement of the peak resistance has been observed, with, however, an enhancement of the ultimate ductility in the case of curved specimens, which delays the full debonding.

This behavior is inherent to the layered nature of FRCM systems. The spike is turned through the fiber grid and fanned within the external mortar layer, which is subjected to positive normal stresses and cracks at early loading stages, preventing an effective load transfer from the fiber grid to the spike. As a result, the spike does not act as a strengthening device, but rather as a kinematic barrier that delays the activation of debonding in the reinforcement portion between the spike and the free edge. At the global level, debonding first develops between the loaded edge and the spike, similarly to unanchored specimens, followed by slippage of the fiber bundles in the rear segment.

Lacking numerical models available for FRCM reinforced stack bond masonry prisms in the presence of spikes, to contextualize the importance of the topic, there is therefore the need to refer to the numerical literature dealing with the debonding behavior of FRCM reinforced specimens without anchor spikes, mostly flat and less frequently curved. To the best of the authors' knowledge, two main approaches are the most diffused, namely (i) those lumping nonlinearity at the reinforcement-support interface and (ii) those modelling separately the different layers, with mutual interactions by means of interfaces.

As far as the first set of approaches is concerned, it relies on idealizing the reinforcement with an elastic layer of fiber and a non-linear interface between FRCM and support. Experimental information may be useful to tune the mechanical properties of the interface, with the possibility to deduce a suitable stress-slip law from the measurement of the slip at the loaded edge [28]. This is an important issue for FRCM reinforcement, where it is not possible to monitor the fiber strains along the bonded length, because of the presence of the external matrix that hides the central layer, unless optic fibers are embedded inside the reinforcement [15]. It is also interesting to point out that the assumption of multi-linear [36] or exponential-softening laws [15,47] for the interface allows for obtaining closed-form solutions in the case of flat specimens. On the contrary, when curved substrates are considered, the utilization of numerical approaches seems the only viable option.

This is the reason why, in some other publications, see e.g. [28], the field problem (which mathematically translates into a second-order differential equation) is solved as a standard Boundary Value Problem BVP, or less frequently, transformed into a Cauchy's Initial Value Problem IVP [15], which has the advantage of being fully explicit.

Actually, if literature focusing on lumping all nonlinearities into a single fictitious interface is moderate in numerosity, the approaches belonging to the second set, which require a distinct modeling of the FRCM's different layers, are even fewer.

For example, in [22], a sophisticated approach was proposed, where the elastic reinforcing grid and the internal brittle matrix were modeled separately, and they interacted with a nonlinear interface. An anelastic system of differential equations was obtained, transforming a standard BVP into an IVP, then solved with a classic shooting technique. The idea of disregarding one of the mortar layers is common with [19], where, however, the matrix layer was assumed to be elastic-perfectly fragile. A step forward in this regard was achieved in [39], where all the layers were modeled, and the field problem was defined by a system of three second-order differential equations, necessitating a 2D shooting. Whilst the procedures turn out to be rather appealing, because they can give locally much more information on the debonding phenomenon in FRCM reinforced specimens, their practical use in common design appears tricky because the direct implementation into FE software is non-obvious.

Speaking about FEs, they can be used in simulating the debonding test, see e.g. [26,35]. Typically, the standard galleries of elements and material models available are utilized, but this clearly constrains the user to carry out computations with a commercial code that is not tailored for a highly complex and peculiar mechanical problem, such as the present one.

From the above considerations, it is noticeable that reliable models for specimens equipped with spikes seem still missing.

Beyond the specific constitutive assumptions and the simplified representation of the spike, the main contribution of the present work lies in the development of a coherent, low-dimensional framework aimed at mechanically interpreting the experimentally observed two-stage debonding mechanism, rather than merely fitting global force–displacement responses.

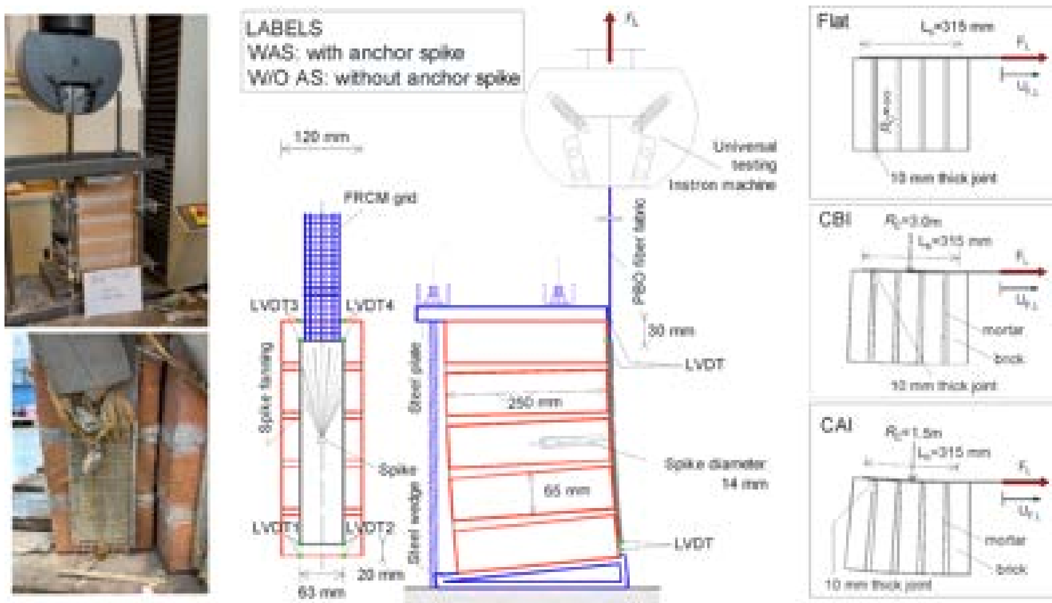

Fig. 1. Experimentation carried out in [44], single lap shear tests of PBO-FRCM reinforced curved masonry pillars with anchor spikes.

Table 1
Characteristics of the specimens: geometry and spike anchor layout. (* turned up and fanned on the fiber layer; ** turned up and fanned on the outer matrix layer)

series	# spec.	Internal radius [mm]	Bonded length [mm]	Spike anchor presence	Reference (experimental data)
Flat WAS	3*+3**	∞	315	yes	[44]
CAI WAS	3*+3**	1500	315	yes	[44]
CBI WAS	3*+3**	3000	315	yes	[44]
Flat W/O AS	6	∞	315	no	[30]
CAI W/O AS	6	1500	315	no	[30]
CBI W/O AS	6	3000	315	no	[30]

* spike turned up and fanned on the fiber layer.
** spike turned up and fanned on the outer matrix layer.

The present paper partially fills this gap by proposing a simplified interface-based model aimed at reproducing the main experimental features with limited computational effort. All nonlinear behavior is lumped at the reinforcement–substrate interface, described through a trilinear shear stress–slip law with elastic, softening, and residual stages. The effect of curvature is accounted for by a frictional–cohesive formulation linking the interface response to curvature-induced normal stresses.

The spike is modeled as a linear spring connecting the reinforcement portions located between the free and loaded edges. Assuming a rigid substrate, the fiber axial displacement coincides with the interface slip, leading to a standard second-order nonlinear differential problem in terms of slip. The formulation allows the problem to be solved explicitly through a sequential Cauchy approach, efficiently handled by a Runge–Kutta scheme.

Comparison with an experimental campaign on laboratory-scale curved masonry prisms assembled from stacked units and mortar layers reinforced with FRCM and equipped with a central spike shows that the model captures the dominant trends, highlighting the role of curvature in reducing peak strength while enhancing post-peak ductility, as well as the limited contribution of the spike to peak load enhancement.

2. Recaps of the experimental tests carried out

In the present section, a brief recall of the experimental results presented by the authors in [44] is provided. A premise is indeed necessary, because such data are used in the final section to validate the numerical model proposed. For a comprehensive discussion of the experimental campaign carried out, the reader is referred to [44]. On the contrary, here the basic observations done on the failure mechanisms triggered and a brief description of the experimental apparatus used are reported to justify the hypotheses done in the simplified numerical model proposed afterward.

The experimental program relied on single-lap shear tests performed on FRCM reinforced curved stack bond masonry prisms (for consistency with the terminology adopted in the authors' previous experimental works, these specimens are hereafter conventionally referred to as "pillars", although they do not represent structural pillars in the strict sense), intended to gain an insight into the influence of spike anchors on the bond behavior of PBO-FRCM reinforcements applied to masonry substrates exhibiting different curvatures. The geometric characteristics of the samples and an overview of the experiments carried out are provided, respectively, in Fig. 1 and Table 1.

Labels used have the following meaning: Flat indicates the flat case, whereas CA and CB refer to curved configurations, characterized respectively by curvature radii equal to 1500 mm and 3000 mm. The "I" letter in the labels indicates that the reinforcement was applied at the intrados.

The test procedure and specimen geometries were identical to those considered in a previous investigation by the authors in the absence of anchor spikes [30], which are also considered for validation purposes.

A total of 18 tests were carried out. For the anchored configurations (WAS), each geometry included six tests divided into two subgroups of three specimens, characterized by two different spike turning-up/fanning procedures (3* + 3** in Table 1). For more details on the latter two different techniques of spike's application, the reader is referred to [44]. For the unanchored configurations (W/O AS), six nominally identical replicates were tested for each geometry.

The masonry samples were built assembling 5 solid clay bricks (dimensions 250 × 120 × 65 mm^3), bonded with mortar, having a thickness at the intrados equal to 10 mm.

The mechanical properties of the PBO-FRCM system reported herein are not derived from the present experimental campaign, but are taken from manufacturer datasheets and from previous experimental characterizations already reported by four of the authors in [30]; accordingly, Table 1 reports geometric and testing parameters only. It consisted of an

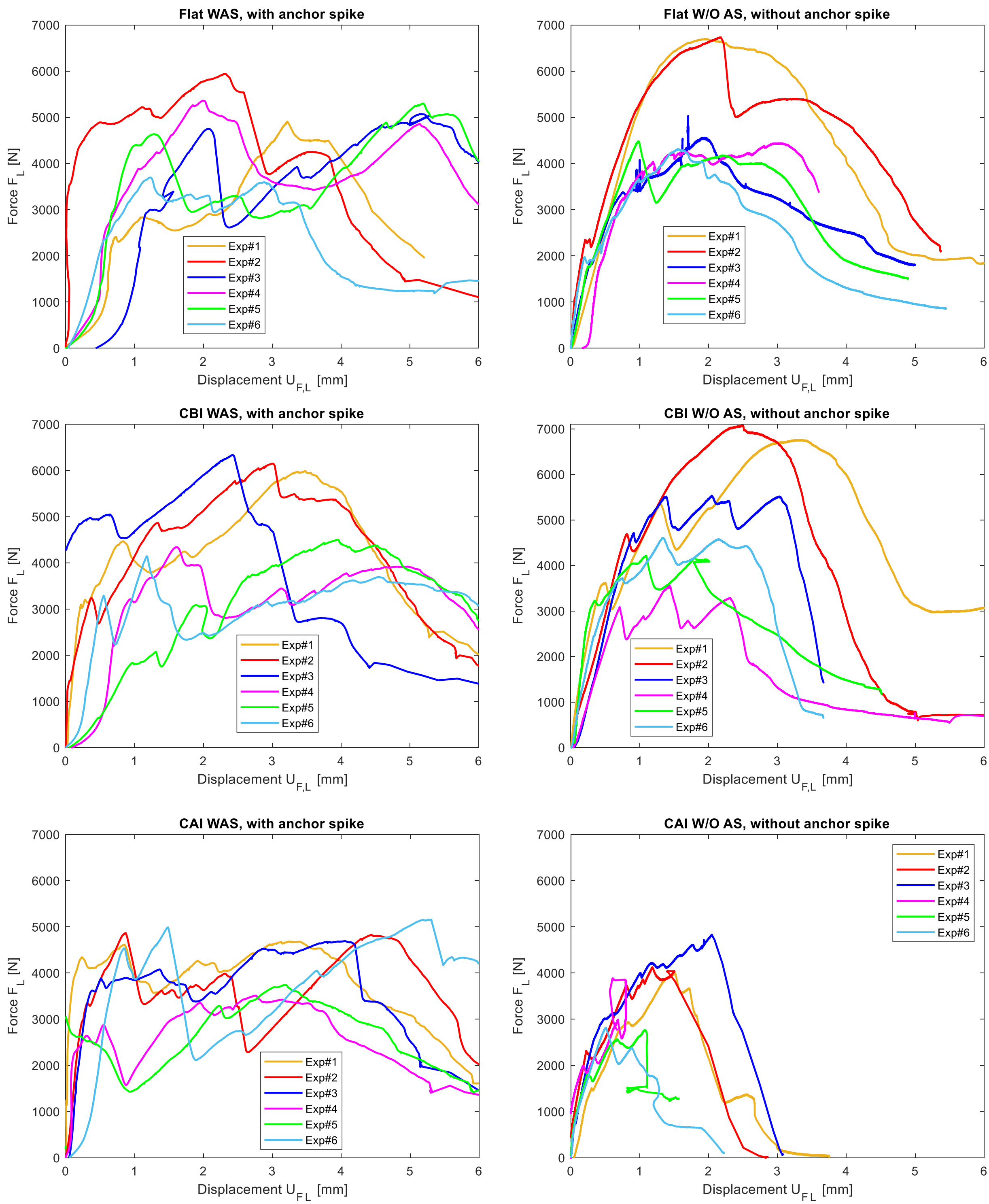

Fig. 2. Experimental results (force-displacement curves) obtained in [30] and [44] for flat and curved masonry pillars reinforced with PBO-FRCM in the presence (left) and absence (right) of anchor spikes in single lap shear tests. The upper bound of the displacement interval is set to 6 mm to facilitate comparisons, and having observed that most of the samples exhibited almost full debonding.

open mesh of polyparaphenylene benzobisoxazole fibers embedded in a cement-based matrix. The mesh had a nominal weight of 94 g/m^2, tensile strength of 5800 MPa, and yarn spacing of 10 mm.

All specimens tested in [44] included one spike anchor made of bundled PBO fibers, inserted at mid-bond length through a drilled hole perpendicular to the surface. The embedment depth was approximately 150 mm.

Shear-lap tests were performed under displacement control using a universal testing machine. Fig. 2 shows the force-displacement curves obtained from the shear-lap tests on both anchored (plots on the left) and unanchored (plots on the right) specimens.

For the tests carried out with spikes, all specimens exhibited a clear two-stage response. During the tests, it was observed that in the first stage, the bonded length between the loaded end and the spike anchor carried the load until the first peak. Then, localized damage in the fan region led to the mobilization of the rear bonded length, producing either a second peak or a plateau before the final softening phase.

The displacement axis in Fig. 2 is intentionally limited to 6 mm to ensure a consistent comparison among different configurations and to focus on the response range that is most relevant for the discussion of the force transmission mechanism and the onset of the second-stage behavior. Furthermore, authors observed that, for most of the samples, almost full debonding occurred before or near 6 mm.

It should be noted that a significant scatter is observed among experimental replicates, especially in the anchored configurations, induced by many factors, such as the presence of different materials exhibiting brittle behavior, the variability of matrix cracking, the local anchor-related damage mechanisms, and a complex stress redistribution, especially near the spike. For this reason, when the performance of the numerical model is assessed against experimental outcomes, we refer to the experimental envelope and to representative scalar quantities (e.g., peak load, slip at peak, and ultimate slip), rather than to a pointwise average of the entire curves.

Overall, compared with unanchored behavior, the spike anchor consistently (i) increased ultimate slip, (ii) reduced the slope of the softening branch, and (iii) promoted secondary mobilization/plateau effects, benefits that were more pronounced in high curvature samples. These trends support the idea that anchors improve post-peak ductility and energy dissipation without necessarily increasing peak strength, which is advantageous for seismic applications in arches and vaults.

No clear clustering of the experimental responses can be identified with respect to the two-spike turning-up/fanning procedures (3* and 3**), as the corresponding force–displacement curves are largely intermingled, and the observed scatter is dominated by installation-related variability rather than the specific turning-up configuration.

It is worth noting that, for flat and low-curvature specimens, the presence of a spike anchor does not necessarily increase the peak load and may even lead to slightly lower maximum forces. This behavior reflects the limited ability of the spike to transfer tensile forces in FRCM systems prior to extensive matrix cracking.

Finally, it is also evident from plots that some experimental curves exhibit markedly different initial stiffnesses, especially in the presence of spike anchors. This behavior is attributed to early-stage effects such as local seating of the testing setup, initial closure of micro-cracks in the mortar layers, and variability in spike installation and fanning conditions. These phenomena mainly influence the very initial portion of the response and do not affect the subsequent force transfer mechanisms governing peak load and post-peak behavior, which are the focus of the present modeling approach.

3. Numerical model proposed, a phenomenological approach

This section describes the main features of the simplified numerical model proposed, aimed at predicting the role played by spikes in the reinforcement of masonry curved pillars.

The model discussed has a phenomenological nature, namely, it is deduced in its assumptions by the behavior experimentally observed and described in the previous section, especially as far as the failure modes triggered in the presence and absence of anchor spikes are concerned.

To understand the rationale at the base of the hypotheses done, a premise on the general meaning of phenomenological or mechanistic models is believed to be beneficial for the reader.

Xu [48] notes that in the mechanics of materials two alternative modeling approaches are frequently used, also known as phenomenological or micro–macro. The first, used here, describes empirical relationships among macroscopic phenomena in line with mechanical laws, without microscopic information or statistics. In this regard, a mechanistic model can be defined as phenomenological if it omits explicit microscopic details. Joseph [49] adds that such models typically involve three steps: the first relies in selecting state variables and constitutive parameters, the second formulates a mathematical description of the observed phenomenon, and finally the third measures and validates experimentally the parameters. It is important to underline that the selection of the state variables and of the constituent parameters is typically done after the experimental observation of the phenomena occurring macroscopically. The previous statement means also that a phenomenological model accounts for the observed behavior without modeling the underlying physical processes. In complex problems like the present one, it is often convenient to start by modeling the observed behavior and later to proceed investigating the likely physical basis.

The previous considerations fit the general problem of seeking suitable representations of phenomena and their mechanistic explanations [50,51]. In this general framework, the derivation of the governing equations for the problem at hand is based on a one-dimensional membrane equilibrium of the reinforcement. The FRCM strip is idealized as a linearly elastic axial member, and bending effects, transverse shear deformation, and geometric nonlinearity of the reinforcement are neglected. This assumption is consistent with the single-lap shear test configuration, where the response is dominated by axial stress transfer along the bonded length.

The masonry substrate is assumed rigid and infinitely resistant, so that all relative displacement is concentrated at a fictious reinforcement–substrate interface, assumed to behave non-linearly. It should be emphasized that the equivalent zero-thickness interface adopted in the present formulation does not represent a purely local constitutive layer. Rather, it provides an effective description that accounts for the combined effects of matrix cracking, fiber–matrix interaction, and progressive debonding observed experimentally in FRCM systems. It therefore meets perfectly the general definition given above for a phenomenological approach, renouncing in providing local/micro information. It may be also considered a classic procedure that has gathered quite a following in the specialized literature, see e.g. [52–58], and whose validity is nowadays taken for granted.

It is worth noting that, despite the phenomenological nature of the formulation, the model is not intended as a mere parameter-fitting tool. The governing equations are derived from mechanical equilibrium and compatibility conditions, and the adopted constitutive relationships retain a clear physical interpretation. As a result, the model provides a mechanically grounded reduced-order representation of the problem, rather than an empirical curve-fitting approximation.

Although all nonlinearities are lumped into a single interface law, different stress-transfer mechanisms are explicitly considered at different locations along the bonded length through the distinction between unloaded (L) and loaded (R) segments. In particular, fiber sliding within a cracked matrix governs the response near the free edge and the spike, whereas curvature-induced normal stresses play a dominant role closer to the loaded edge. The proposed lumped formulation is therefore meant to capture these location-dependent mechanisms in an averaged manner, remaining mechanically consistent, rather than reproducing each local damage process explicitly.

It is important to emphasize that the present formulation does not aim at providing a fully rigorous mechanical description of all local damage mechanisms involved in the debonding process. Instead, it represents a simplified and internally consistent framework designed to capture the dominant global response features governing the two-stage behavior observed experimentally.

Accordingly, the validity of the proposed model is restricted to cases where interface-governed mechanisms prevail, while more complex three-dimensional effects, such as through-thickness damage, local cracking patterns, or peeling phenomena, are only indirectly accounted for through the adopted equivalent interface law.

Accordingly, the proposed model is intended to simulate interface-governed debonding mechanisms in FRCM-strengthened masonry

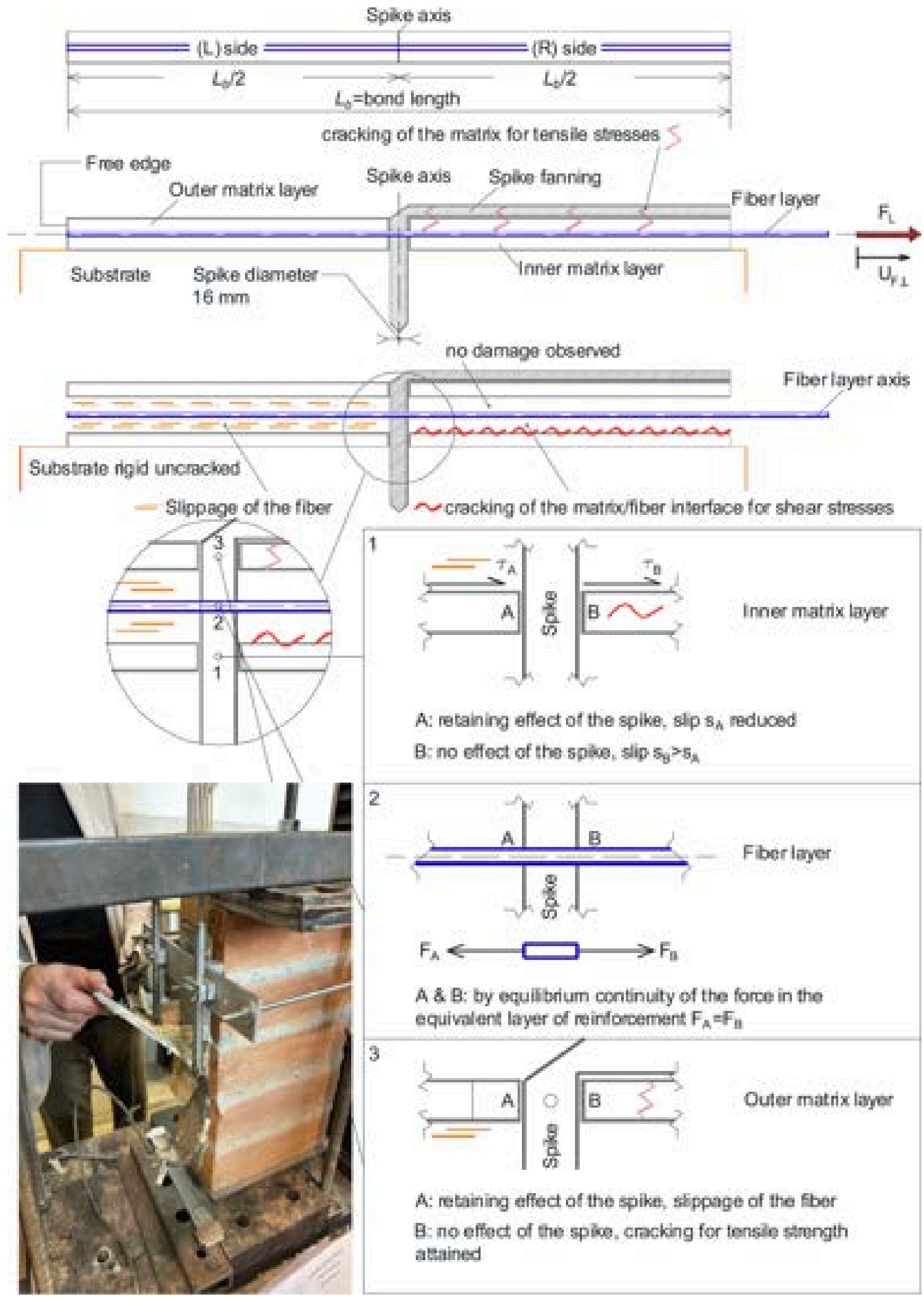

Fig. 3. Experimental observations of the failure mechanism developing in the FRCM reinforcing system in the presence of a spike.

elements, with fiber rupture, spike pull-out, and crushing of the substrate explicitly excluded from the failure modes considered.

In compliance with the previous definition of phenomenological approach, local sources of non-linearity such as cracking and damage of the outer mortar layer, progressive fiber–matrix debonding, local stress concentrations around the spike, and frictional sliding of fiber bundles within a cracked matrix are not modeled explicitly, but are incorporated equivalently through the calibrated shape and parameters of the interface shear stress–slip law.

The curvature of the support is assumed uniform along the bonded length, as in the experimental specimens considered, and its effect is introduced exclusively through the normal stress acting at the interface. A positive sign of the interface normal stress refers to intrados applications, corresponding to detachment-prone configurations characterized by tensile normal stresses at the interface, while negative values correspond to extrados reinforcement. The proposed formulation is therefore applicable to single-lap shear problems involving small-to-moderate curvatures, where the bending stiffness of the reinforcement and curvature variation along the bonded length can be reasonably neglected. In practical terms, the validity of these assumptions is expected to hold for curvature levels comparable to those investigated experimentally in this study, where the radius of curvature is large with respect to the bonded length and the reinforcement response remains dominated by axial stress transfer rather than bending effects.

As experimental evidence suggests, the anchor plays a role that is non-obvious and certainly different from that introduced in a reinforcement with FRP [40–42], due to the higher complexity of the FRCM, which is constituted by three layers (inner and outer matrix, and central fiber).

In the FRP-based model proposed in [40], the reinforcement is assumed as a continuous laminate bonded to the substrate through an adhesive layer capable of efficiently transferring tensile stresses. In that framework, the spike anchor provides a direct load-transfer mechanism to the FRP laminate and contributes significantly to the peak strength, resulting in a clear second load-bearing stage.

In contrast, the present model reflects the intrinsic layered nature of FRCM systems. The spike is installed through the fiber grid and fanned into the outer mortar layer, which is subjected to tensile normal stresses in intrados applications and cracks at very early loading stages. Consequently, the spike is unable to effectively transfer axial force to the fiber layer. Its mechanical role is therefore interpreted as a kinematic constraint that delays the debonding of the rear bonded length, rather than as a strength-enhancing element.

This fundamental difference in force transmission explains why, unlike FRP systems, FRCM reinforcements equipped with spike anchors exhibit only marginal changes in peak load, while showing a more pronounced effect in terms of post-peak response and ultimate slip, particularly for curved substrates.

In Fig. 3, the third sub-figure from the top highlights the markedly different failure mechanisms developing on the unloaded (L) and loaded (R) sides of the spike. On the loaded side (R), cracking and debonding occur at the inner matrix–fiber interface, similarly to unanchored specimens, whereas on the unloaded side (L), a clear slippage of the fiber bundles within the matrix is observed.

In particular, the following considerations on both technological aspects and experimental observations may be drawn:

1) The inner matrix is interrupted by the spike. Its stiffness limits the displacement of the inner matrix near the free edge, while the portion closer to the loaded edge remains almost unaffected.
2) The spike passes through the central fiber net without interaction. It is therefore reasonable to infer that the displacement field of the central layer remains unaltered by the anchor presence.
3) As the spike fans into the outer matrix on the loaded side, and this outer mortar layer is fully in tension and cracks early, the shear transfer between the fanned spike and the FRCM may be considered negligible.
4) The failure mechanism observed is different between the portion of reinforcement located on the unloaded side (L) with respect to the central spike and that on the loaded one (R) – left and right portions, as shown in the paper's figures. In particular, the loaded side fails in the same manner observed without a spike, i.e., with cracks propagating at the inner matrix/fiber interface, whereas the unloaded one exhibits a clear slippage of the central PBO fibers with respect to the matrix.

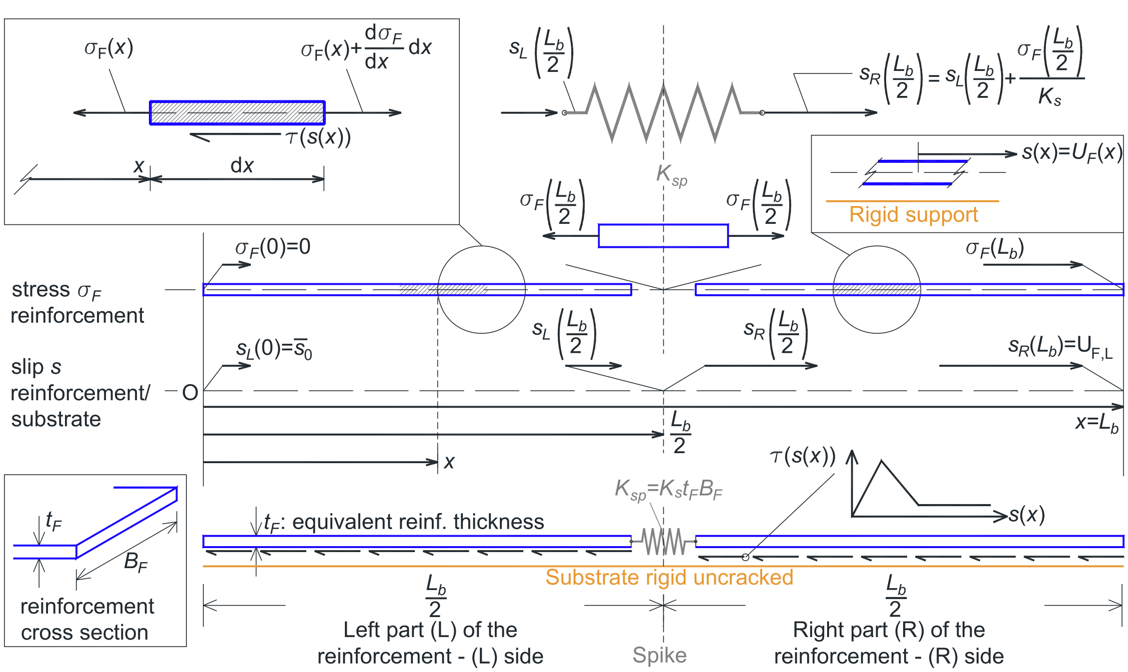

Fig. 4. Simplified mechanical model proposed.

According to such considerations, the FRCM reinforcement (inner and outer matrices with fiber) is assumed to be linear elastic and bonded to the substrate through a single equivalent non-linear interface.

Fig. 4 schematically illustrates the phenomenological one-dimensional model adopted. The main diagram shows the bonded length, the subdivision into unloaded (L) and loaded (R) segments, and the spike modeled as an axial spring along the bonded length. Such idealization appears convenient because it reflects simply the role played by the spike, i.e., to promote a slip discontinuity between the unloaded and loaded segments.

The bottom-left subfigure represents a cross-sectional view of the FRCM reinforcement, highlighting the idealization of the fiber layer as an equivalent elastic strip interacting with the substrate through a zero-thickness interface. The distinction between the L and R segments reflects the different dominant failure mechanisms observed experimentally on the two sides of the spike.

Consequently, as far as the non-linear interface between FRCM reinforcement and substrate is concerned, different constitutive laws should be adopted. In particular, on the unloaded side, governed by fiber-bundle slippage, curvature has no effect; that is, the tau–slip law is insensitive to the normal stress at the interface. On the loaded side, the response matches that of specimens without anchors, so the normal stress induced by curvature must be included.

According to the previous considerations and with reference to the symbols reported in Fig. 4, let us assume that the support is rigid and infinitely resistant and that the reinforcement is constituted by an elastic material with equivalent thickness equal to t_F (width equal to B_F), and elastic modulus E_F. Let us also assume that the bond length is equal to L_b, and that the spike is installed at the middle length, i.e., at a distance equal to $L_b/2$ from both the free and the loaded edges, located respectively on the left and on the right sides.

A one-dimensional coordinate x along the bonded length is defined, with $x = 0$ at the free edge and $x = L_b$ at the loaded edge.

With a rigid substrate, the local slip $s(x)$ equals the reinforcement axial displacement $U_F(x)$ and varies along x.

The reinforcement transfers shear stresses τ to the substrate through a non-linear bond interface governed by a trilinear $\tau - s$ law.

According to the symbols reported in Fig. 5, the $\tau - s$ interface behavior is ruled by the following equations:

$$\tau(s) = \begin{cases} 0 \le x \le \dfrac{L_b}{2} & \begin{cases} \tau(s) = \dfrac{\tau_{L,sM}}{s_{L,se}} s & 0 \le s \le s_{L,se} \\ \tau(s) = \tau_{L,sM} + \dfrac{\tau_{L,sr} - \tau_{L,sM}}{s_{L,su} - s_{L,se}} (s - s_{L,se}) & s_{L,se} < s \le s_{L,su} \\ \tau(s) = \tau_{L,sr} & s > s_{L,su} \end{cases} \\ \dfrac{L_b}{2} < x \le L_b & \begin{cases} \tau(s) = \dfrac{\tau_{R,sM}}{s_{R,se}} s & 0 \le s \le s_{R,se} \\ \tau(s) = \tau_{R,sM} + \dfrac{\tau_{R,sr} - \tau_{R,sM}}{s_{R,su} - s_{R,se}} (s - s_{L,se}) & s_{R,se} < s \le s_{R,su} \\ \tau(s) = \tau_{R,sr} & s > s_{R,su} \end{cases} \end{cases} \tag{1}$$

Symbols in Eq. (1) - in agreement with those reported in Fig. 5- have the following meaning:

- L_b and $\tau(s)$ are respectively the bond length and the shear stress acting at the fiber/substrate interface at position x for a slip equal to s.

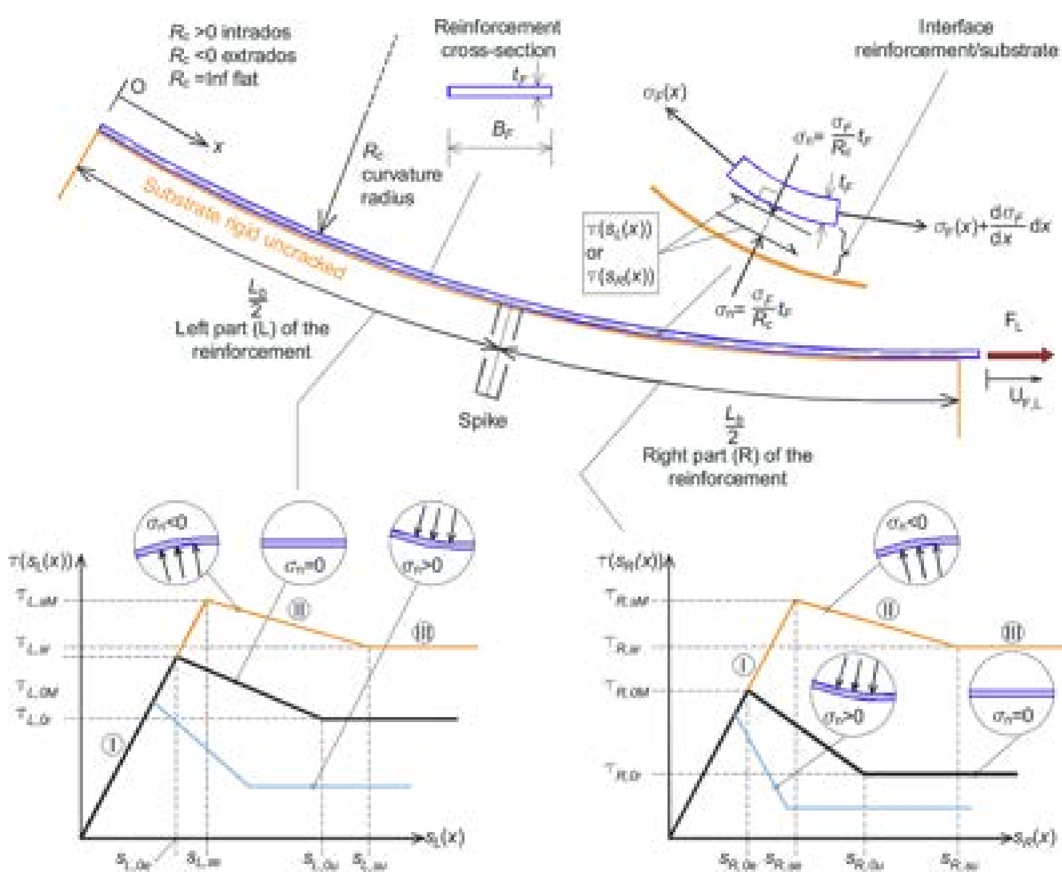

Fig. 5. Effect of the curvature on the shear stress-slip law of the interface between substrate and elastic reinforcement.

- $\tau_{L,sM}(\tau_{R,sM})$ and $\tau_{L,sr}$ ($\tau_{R,sr}$) are respectively the peak and residual tangential strength of the unloaded L (loaded R) interface when a normal stress $\sigma_n \neq 0$ is acting.
- $s_{L,se}(s_{R,se})$ and $s_{L,su}$ ($s_{R,su}$) are the slips corresponding respectively to shear stresses equal to $\tau_{L,sM}$ ($\tau_{R,sM}$) and $\tau_{L,sr}$ ($\tau_{R,sr}$).

Let us also define the following stress and slip quantities:

- $\tau_{L,0M}(\tau_{R,0M})$ and $\tau_{L,0r}$ ($\tau_{R,0r}$), respectively, peak and residual tangential strengths of the unloaded L (loaded R) interface when the normal stress σ_n is equal to zero (flat case).
- $s_{L,0e}(s_{R,0e})$ and $s_{L,0u}$ ($s_{R,0u}$), respectively slips at shear stresses equal to $\tau_{L,0M}$ ($\tau_{R,0M}$) and $\tau_{L,0r}$ ($\tau_{R,0r}$) when $\sigma_n = 0$ (flat case).

In the model proposed, $\tau_{L,sM}$ ($\tau_{R,sM}$) depends on the actual value of σ_n and is linked to $\tau_{L,0M}$ ($\tau_{R,0M}$) according to the following Mohr-Coulomb relationships:

$$\begin{aligned} \tau_{L,sM} &= \tau_{L,0M} + \mu_{L,M}\sigma_n \\ \tau_{R,sM} &= \tau_{R,0M} + \mu_{R,M}\sigma_n \end{aligned} \tag{2}$$

where $\mu_{L,M}$ and $\mu_{R,M}$ are friction coefficients for the unloaded (L) and loaded (R) parts.

In Eq. (2) and in what follows, the sign convention for the interface normal stress is such that positive values of σ_n correspond to intrados applications (detachment-prone configuration), whereas negative values refer to extrados reinforcement. It is worth noting that, for intrados reinforcement, experimental evidence indicates premature cracking of the outer mortar layer and an early loss of effective confinement, so that a positive σ_n induces a reduction of the frictional resistance. Accordingly, the normal-stress dependence introduced in Eq. (2) is formulated to reproduce the observed reduction of peak bond transfer when $\sigma_n > 0$.

The same rationale, with some modifications for the intrados reinforced, is adopted to tune residual tangential stresses, namely:

$$\begin{aligned} \tau_{L,sr} &= \begin{cases} \sigma_n < 0 & \tau_{L,sr} = \tau_{L,0r} + \mu_{L,r}\sigma_n \\ \sigma_n > 0 & \tau_{L,sr} = \tau_{L,0r}e^{-\rho_{L,r}\sigma_n} \end{cases} \\ \tau_{R,sr} &= \begin{cases} \sigma_n < 0 & \tau_{R,sr} = \tau_{R,0r} + \mu_{R,r}\sigma_n \\ \sigma_n > 0 & \tau_{R,sr} = \tau_{R,0r}e^{-\rho_{R,r}\sigma_n} \end{cases} \end{aligned} \tag{3}$$

where $\mu_{L,r}$ ($\mu_{R,r}$) is again a friction coefficient for the L unloaded (R loaded) part and $\rho_{L,r}$ ($\rho_{R,r}$) is a further coefficient (dimension [1/MPa]) which simulates a rapid drop of resistance in the presence of positive normal stresses. With reference to Eq. (3), it is worth highlighting that for $\sigma_n > 0$, an exponential decay term tuned by $\rho_{L,r}$ ($\rho_{R,r}$) is adopted to phenomenologically capture the rapid deterioration of residual/frictional transfer observed experimentally at the intrados due to early mortar cracking. For $\sigma_n \leq 0$, this correction is generally not observed, and the residual response follows the baseline frictional trend.

As far as the ultimate slip is concerned, the following formulas hold for the L unloaded side (nothing changes for the loaded side):

$$\begin{cases} s_{L,0u} = (1+\eta_{L,0})s_{L,0e} \\ s_{L,su} = (1+\eta_{L,s})s_{L,se} \\ \eta_{L,s} = \eta_{L,0}e^{-\rho_{L,\eta}\sigma_n} \end{cases} \tag{4}$$

where the coefficient $\eta_{L,0}$ expresses how much the ultimate slip is larger than the elastic limit when $\sigma_n = 0$. Nothing changes when the interface normal stress is non-zero, but in this case, the non-dimensional parameter $\eta_{L,s}$ is directly derived from the knowledge of $\eta_{L,0}$ and σ_n via the introduction of a further non-dimensional parameter $\rho_{L,\eta}$, which enters in the third exponential law of Eq. (4).

Normal stress σ_n is calculated by equilibrium, see Fig. 5, from the knowledge of the reinforcement tensile stress σ_F, according to the following equation:

$$\sigma_n = \frac{\sigma_F}{R_c}t_F \tag{5}$$

where positive values of R_c refer to cases where the reinforcement is installed at the intrados.

From the previous considerations, it is worth noting that $\rho_{L,\eta}>0$ for $\sigma_n \neq 0$. Indeed, for intrados reinforcement $\sigma_n > 0$ and $\eta_{L,s} < \eta_{L,0}$, whereas for extrados reinforcement $\sigma_n < 0$ and $\eta_{L,s} > \eta_{L,0}$.

The model allows calibration of the interface parameters to reflect different materials and surface conditions. The following section reports a sensitivity analysis and the admissible parameter ranges adopted to avoid non-unique fits.

The field equation is deduced classically [15] imposing the longitudinal equilibrium of an infinitesimal portion of the reinforcement, see Fig. 4. The following standard differential relationship is derived, which governs the debonding problem:

$$\frac{d\sigma_F}{dx} = \frac{\tau(s(x))}{t_F} \tag{6}$$

Considering that the fiber layer is assumed linear elastic, hence $\sigma_F = E_F ds/dx$, it is straightforward to obtain the following second-order nonlinear differential equation governing the debonding problem in the independent variable s:

$$\frac{d^2s(x)}{dx^2} = \frac{\tau(s(x))}{E_F t_F} \tag{7}$$

Which can be further manipulated, yielding the following system of first-order differential equations:

$$\begin{cases} \dfrac{ds'}{dx} = \dfrac{\tau(s)}{E_F t_F} \\ \dfrac{ds}{dx} = s' \end{cases} \tag{8}$$

BCs to apply are the following:

$$\begin{cases} x = 0 & \sigma_F = E_F s' = 0 \rightarrow s'(0) = 0 \\ x = L_b & s(L_b) = U_{F,L} \end{cases} \tag{9}$$

where $U_{F,L}$ is the displacement applied at the loaded edge.

With a central anchor spike, as shown in Fig. 4, the problem requires internal conditions at $x = x_s = \frac{L_b}{2}$. The conditions imposed are: (i) equilibrium in the reinforcement, that is, continuity of the axial force across the spike, and (ii) a slip discontinuity at the fiber-substrate interface equal to the spike extension, governed by the spring law:

$$\begin{cases} x = \dfrac{L_b}{2} & s_L'\left(\dfrac{L_b}{2}\right) = s_R'\left(\dfrac{L_b}{2}\right) \\ x = \dfrac{L_b}{2} & s_L\left(\dfrac{L_b}{2}\right) + \dfrac{s_L'\left(\dfrac{L_b}{2}\right)E_F t_F B_F}{K_{sp}} = s_L\left(\dfrac{L_b}{2}\right) + \dfrac{s_L'\left(\dfrac{L_b}{2}\right)E_F}{K_s} = s_R\left(\dfrac{L_b}{2}\right) \end{cases} \tag{10}$$

where the subscripts L and R refer respectively to the left and right parts (namely unloaded and loaded sides, respectively), K_{sp} is the spike stiffness (unit of measure N/mm), and $K_s = K_{sp}/(E_F t_F)$ is the spike stiffness normalized to the cross-section area of the reinforcement (unit of measure N/mm^3). A discussion on how to define K_s in the numerical model, which is based on experimental data, is provided in Appendix A.

A convenient practical implementation is to consider solving two BVPs, having one boundary in common (the anchor spike):

$$\begin{cases} 0 \le x \le \dfrac{L_b}{2} \begin{cases} \dfrac{ds'_L}{dx} = \dfrac{\tau(s_L)}{E_F t_F} \\ \dfrac{ds_L}{dx} = s'_L \end{cases} & \begin{cases} s'_L(0) = 0 \\ s'_L\left(\dfrac{L_b}{2}\right) = s'_R\left(\dfrac{L_b}{2}\right) \end{cases} \\ \dfrac{L_b}{2} < x \le L_b \begin{cases} \dfrac{ds'_R}{dx} = \dfrac{\tau(s_R)}{E_F t_F} \\ \dfrac{ds_R}{dx} = s'_R \end{cases} & \begin{cases} s_L\left(\dfrac{L_b}{2}\right) + \dfrac{s'_L\left(\dfrac{L_b}{2}\right)E_F t_F}{K_s} = s_R\left(\dfrac{L_b}{2}\right) \\ s_R(L_b) = U_{F,L} \end{cases} \end{cases} \tag{11}$$

The numerical strategy adopted is to transform Eq. (11) into two Cauchy problems (also known as Initial Value Problems, IVPs), solvable in series, and taking advantage of the explicit nature of the Cauchy problem, which therefore guarantees stability and reliability for any kind of non-linear behavior selected for the interface. The procedure consists of solving, in the first step, the unloaded (L) part, and then, in a second step, with the solution found in correspondence with the anchor spike for the L part, to consider the loaded (R) one.

This step represents a crucial point of the proposed numerical formulation. By transferring the displacement boundary condition imposed at the loaded edge to an equivalent slip condition at the free edge, the original problem, consisting of two coupled Boundary Value Problems BVPs for the unloaded and loaded segments, can be reformulated as two Cauchy problems solved sequentially. This transformation allows the use of a fully explicit Runge–Kutta integration scheme, ensuring numerical robustness even in the presence of softening interface behavior, as well as a considerable reduction of the time needed to perform the simulations. In Appendix B, the superior numerical reliability and the much-reduced time needed to perform the simulations are discussed, along with a brief description of a standard BVP implementation of the same problem based on Euler forward finite differences.

It is also worth noting that, if the anchor spike is assumed non-linear, two distinct cases must be treated, depending on whether the spike is modelled as a spring exhibiting hardening or softening. In Appendix C, modelling the spike with the simplest constitutive behavior beyond elasticity (i.e. bilinear for hardening and trilinear for softening) it is shown how Eq. (11) can be still reformulated by means of suitable IVPs.

Nevertheless, although more advanced constitutive laws can be adopted for the spike, including hardening or softening behaviors, the analyses reported in Appendix C indicate that such refinements do not necessarily improve the agreement with experimental results. In particular, the introduction of softening in the spike response leads to a premature loss of load transfer capability, resulting in a global response that deviates from the experimentally observed plateau-like behavior.

Moreover, the identification of additional non-linear parameters for the spike is affected by significant uncertainty, due to the complex and highly variable local mechanisms governing spike activation. For these reasons, the linear elastic assumption is retained as a robust and practically identifiable approximation, capable of capturing the dominant kinematic role of the spike without introducing unnecessary modeling uncertainty.

Returning to the BC transfer of the applied displacement $U_{F,L}$ at L_b when the anchor spike is assumed elastic, the latter is substituted by the imposition of a displacement $\bar{s}_0$ at the free edge as follows:

$$\begin{cases} x = 0 \quad s'_L(0) = 0 \\ x = 0 \quad s_L(0) = \bar{s}_0 \end{cases} \tag{12}$$

where $\bar{s}_0$ is the slip applied at the free edge.

The Cauchy's problem to be numerically tackled for the unloaded part is therefore the following:

$$\begin{cases} \dfrac{ds'_L}{dx} = \dfrac{\tau(s_L)}{E_F t_F} \\ \dfrac{ds_L}{dx} = s'_L \end{cases} \begin{cases} s_L(0) = \bar{s}_0 \\ s'_L(0) = 0 \end{cases} \tag{13}$$

An in-house implementation of a standard Fourth-Order Runge-Kutta (RK4) solver is used. With the position $\boldsymbol{y} = [y_1 \quad y_2]^T = [s_L \quad s'_L]^T$, Eq. (13) can be rewritten as follows:

$$\begin{aligned} &\frac{d\boldsymbol{y}}{dx} = \begin{bmatrix} y_2 \\ \dfrac{\tau(y_1)}{E_F t_F} \end{bmatrix} = \boldsymbol{f}(\boldsymbol{y}) \\ &\boldsymbol{y}(0) = \begin{bmatrix} \bar{s}_0 \\ 0 \end{bmatrix} \end{aligned} \tag{14}$$

Partitioning the bond length (which for the L part is equal to $L_b/2$) with a step size equal to h, $n+1$ knot points are considered, where $n = L_b/2h$ and the abscissa of the i-th node is $x_i = (i-1)h$ with $i = 1, \cdots, n+1$. The solution vector $\boldsymbol{y}_{i+1}$ for the knot x_{i+1} is calculated by means of the following fully explicit algorithm, knowing the solution $\boldsymbol{y}_i$ at x_i:

$$\begin{aligned} &\boldsymbol{k}_1 = h\boldsymbol{f}(\boldsymbol{y}_i, x_i) \\ &\boldsymbol{k}_2 = h\boldsymbol{f}\left(\boldsymbol{y}_i + \frac{\boldsymbol{k}_1}{2}, x_i + \frac{h}{2}\right) \\ &\boldsymbol{k}_3 = h\boldsymbol{f}\left(\boldsymbol{y}_i + \frac{\boldsymbol{k}_2}{2}, x_i + \frac{h}{2}\right) \\ &\boldsymbol{k}_4 = h\boldsymbol{f}(\boldsymbol{y}_i + \boldsymbol{k}_3, x_i + h) \\ &\boldsymbol{y}_{i+1} = \boldsymbol{y}_i + \frac{\boldsymbol{k}_1 + 2\boldsymbol{k}_2 + 2\boldsymbol{k}_3 + \boldsymbol{k}_4}{6} \end{aligned} \tag{15}$$

It is worth noting that Eq. (15) is a classic fourth-order Runge-Kutta (RK4) method. As is well known, it is fully explicit, so any kind of non-linearity for the interface can be considered without the risk of premature halting. Furthermore, the error introduced is always an $O(h^5)$. The solution can be found very rapidly -also because the system of differential equations has size equal to 2-, so h can be set extremely small. For instance, in the simulations reported hereafter h is assumed equal to $10^{-4}L_b/2$.

A final remark pertains the way terms $\boldsymbol{f}\left(\boldsymbol{y}_i + \frac{\boldsymbol{k}_1}{2}, x_i + \frac{h}{2}\right)$, $\boldsymbol{f}\left(\boldsymbol{y}_i + \frac{\boldsymbol{k}_2}{2}, x_i + \frac{h}{2}\right)$ and $\boldsymbol{f}(\boldsymbol{y}_i + \boldsymbol{k}_3, x_i + h)$ are computed in Eq. (15). Indeed, according to Eq. (14), the first row of $\boldsymbol{f}$ is equal to $\frac{\tau(y_2)}{E_F t_F}$, but $\tau(y_2)$ is actually dependent also on σ_n, which in turn is a function of y_2. More precisely:

$$\sigma_n = \frac{E_F t_F}{R_c} y_2 \tag{16}$$

Rigorously, one should calculate σ_n with the solution at $\boldsymbol{y}_i + \frac{\boldsymbol{k}_1}{2}$, $\boldsymbol{y}_i + \frac{\boldsymbol{k}_2}{2}$ and $\boldsymbol{y}_i + \boldsymbol{k}_3$, but the authors experienced -thanks to the very small step size assumed- negligible differences if the value of σ_n at x_i is adopted.

Once the solution for the unloaded side is retrieved using Eq. (15), the loaded one is solved numerically in the same way, considering the following Cauchy problem:

$$\frac{d\boldsymbol{y}}{dx} = \begin{bmatrix} y_2 \\ \dfrac{\tau(y_1)}{E_F t_F} \end{bmatrix} = \boldsymbol{f}(\boldsymbol{y})$$

$$\boldsymbol{y}\left(\frac{L_b}{2}\right) = \begin{bmatrix} s_L\left(\dfrac{L_b}{2}\right) + \dfrac{s_L^{'}\left(\dfrac{L_b}{2}\right)E_F t_F}{K_s} \\ s_L^{'}\left(\dfrac{L_b}{2}\right) \end{bmatrix} \tag{17}$$

where $s_L\left(\frac{L_b}{2}\right) = y_1^{n+1}$ and $s_L^{'}\left(\frac{L_b}{2}\right) = y_2^{n+1}$ computed for the last knot $n+1$ in Eq. (15).

According to the previous calculation scheme, the global force–displacement curve is thus generated by prescribing a sequence of increasing values of the slip at the free edge $\bar{s}_0$ and solving the resulting Cauchy problems by means of the aforementioned RK4 scheme. For each imposed $\bar{s}_0$, the corresponding displacement at the loaded edge $U_{F,L}$ and the applied force $F_L = \sigma_F(L_b)E_F t_F$ are obtained as outputs of the solution. Neither iterative equilibrium nor arc-length procedures are employed, and the response is traced within a fully explicit kernel under displacement control of the slip applied at the free edge.

4. Results

The simplified numerical model discussed in the previous section is here benchmarked with reference to the experimental setup briefly recalled in Section 2. Mechanical properties of the interface between reinforcement-substrate and adopted for the unloaded (L) and loaded (R) bonded parts are summarized in Table 2. It is worth mentioning that the data provided in Table 2 for the R part are in close agreement with those used by Grande and co-workers [37], since in Pingaro et al. [44] the experimental tests have been carried out on specimens built with the same materials and the same geometries discussed by Grande et al. [37]. To account for the spike, which changes the failure mode between the free edge and the anchor, the L segment uses the same interface parameters but with a $\tau - s$ law that does not depend on the local normal stress σ_n. This choice reflects the observed mechanism in that region, where fiber sliding within the matrix governs the response rather than curvature-induced normal stresses. In other words, the experimental failure mechanism does not exhibit any peeling detachment triggered by the unavoidable pull-off normal stresses present, ruled by equilibrium via Eq. (5). Despite the latter may be non-negligible at late stages of the deformation process, even near the free edge, they are not responsible for visible normal detachments from the substrate. Indeed, the presence of the anchor, when the part towards the free edge is considered, physically precludes peeling, at least at the location of the spike. On the other hand, as far as the left part is concerned, normal stresses attain the largest values in the near-spike region, so it is reasonable to infer that the part towards the free edge is not subjected to spalling anywhere. It is also important to point out that the proposed phenomenological model is native one-dimensional, with failure possible only in pure mode II. Consequently, no normal displacement jumps can be derived from the model, and the only way to account for the role of curvature is to modify the interface shear stress-slip relationship, following a Mohr–Coulomb behavior, as widely done in the literature and as previously discussed.

To summarize, although curvature-induced normal stresses are present along the bonded length, including near the spike, their effect on the global response is not governed by the activation of mode I debonding mechanisms, which are not observed experimentally. Instead, their contribution is indirectly accounted for through the modification of the interface shear behavior via the Mohr–Coulomb formulation adopted for the loaded segment.

Moreover, as it will be shown later, numerical results obtained by enforcing identical constitutive laws on both sides of the spike show a deterioration of the agreement with experimental data, indicating that explicitly introducing normal-stress effects in the unloaded segment does not improve the predictive capability of the model.

In the absence of the spike, all the bonded length should be assumed to obey the constitutive law of the loaded (right) part. Hence, the proposed model can be also used to simulate the debonding test without spike, simply adopting the previous modification for the interface and augmenting stiffness K_s of the anchor at infinite.

In all those cases when the spike is present, in the absence of specific experimental data, K_s is assumed equal to 4960 N/mm^3, according to the procedure described in Appendix A.

It is worth noting that the present formulation does not aim at resolving highly localized damage phenomena in a pointwise sense, such as crack initiation and propagation in the outer matrix layer near the spike. These effects are inherently smeared within the equivalent interface description. Nevertheless, the spatially localized nature of the response is partially captured through the subdivision of the bonded length into unloaded (L) and loaded (R) segments, each governed by distinct interface laws reflecting different dominant stress-transfer mechanisms. As a result, the model can reproduce the main consequences of localization on the global response—such as delayed debonding, post-peak behavior, and increased ultimate slip—while sacrificing the detailed description of local damage patterns.

In Fig. 6, the shear stress-slip relationship of the interfaces between reinforcement and substrate is depicted with data of Table 2 at three values of σ_n, equal to 0, 0.1, and -0.1 MPa. As already pointed out, the L part (Fig. 6-a) is insensitive to σ_n, whereas the R part (Fig. 6-b) increases or decreases ductility and peak strength depending on whether the reinforcement is installed at the extrados or intrados, respectively.

To set the other geometric and mechanical properties necessary to fully define problem (11) the following values are assumed, again in agreement with [30,36–39]: fiber elastic modulus $E_F = 241000$ MPa and $t_F = 0.05$ mm. To evaluate the loaded edge force F_L it is also necessary to set the equivalent out-of-plane width of the reinforcement B_F, which is assumed here equal to 25.2 mm. Both B_F and t_F are conventional geometric quantities calculated from a rough estimation of the bundles' cross area A_F (1.26 mm^2, resulting from the area of 7 bundles with elliptic cross section with semi-axes equal to 0.0286 mm and 2 mm) and its semi-perimeter $p_F = B_F$, again with calculations made in agreement with [28], so that $t_F = A_F/p_F$).

It is worth noting that, unlike common practice based on the textile areal weight, the equivalent thickness t_F and width B_F are here defined from a mechanical standpoint, starting from an estimation of the effective cross-sectional area of the fiber bundles. This choice reflects the discrete nature of FRCM systems, where axial force is mainly carried by individual bundles rather than a continuous laminate, and is consistent with the simplified one-dimensional formulation adopted. The present definition ensures a correct representation of axial stiffness and curvature-induced normal stresses within the interface-based model, while avoiding assumptions that are not representative of the actual stress transfer mechanisms in cracked cementitious matrices.

Table 2
Mechanical properties assumed for the unloaded (Left L) and loaded (Right R) bonded parts to analyze FRCM-reinforced curved masonry pillars in the presence of an anchor spike.

Left bonded part L			Right bonded part R		
$\tau_{L,0M}$	1.75	MPa	$\tau_{R,0M}$	1.75	MPa
$\tau_{L,0r}$	0.35	MPa	$\tau_{R,0r}$	0.35	MPa
$s_{L,0e}$	0.065	mm	$s_{R,0e}$	0.065	mm
$s_{L,0u}$	0.42	mm	$s_{R,0u}$	0.42	mm
$\mu_{L,M}$	0	-	$\mu_{R,M}$	0.58	-
$\mu_{L,r}$	0	-	$\mu_{R,r}$	0.18	-
$\rho_{L,r}$	0	MPa^{-1}	$\rho_{R,r}$	8	MPa^{-1}
$\rho_{L,\eta}$	0	MPa^{-1}	$\rho_{R,\eta}$	6	MPa^{-1}

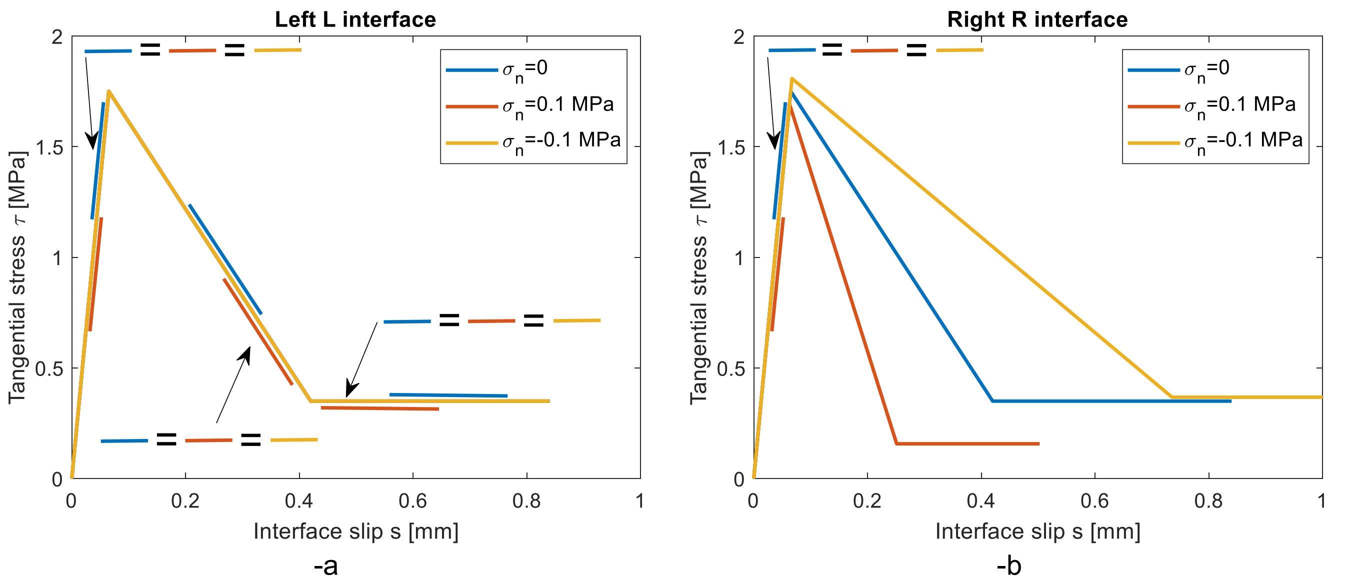

Fig. 6. Constitutive behavior of the unloaded L (-a) and loaded R (-b) interface at three different levels of normal stress $\sigma_n = 0$ (Flat case), $\sigma_n = -0.1$ MPa (extrados reinforcement) and $\sigma_n = 0.1$ MPa (intrados reinforcement).

Fig. 7 compares the global force–displacement curves for flat specimens with and without the spike, against the experimental envelope.

It should be noted that the numerical curves exhibit snap-back branches, which are a direct consequence of the softening interface behavior captured by the model. In displacement-controlled experimental tests, such unstable equilibrium paths cannot be followed, and therefore, the comparison with experimental data refers exclusively to the stable branch of the numerical response. The snap-back behavior, however, remains mechanically meaningful, as it reflects the energy dissipation mechanisms associated with progressive debonding and interface softening. The same inability to capture snap-back is observed for all those numerical models formulated as BVPs, because a monotonic increase of $U_{F,L}$ is imposed at the loaded edge. For further details, the reader may refer to Appendix B.

Fig. 7 also shows that, for the flat case, the spike does not increase the peak load and produces only a marginal change in the ultimate slip. The model reproduces the two-stage response observed experimentally: after the first peak, a transient drop in load occurs when the bonded length between the loaded end and the spike fully de-bonds, followed by the delayed mobilization of the rear bonded length. The numerical response captures the main experimental trends and falls within the overall experimental scatter in terms of stiffness level, peak activation sequence, and post-peak evolution, although noticeable discrepancies in peak load and ultimate displacement remain.

It should be noted that, in the flat configuration without anchor spikes (Fig. 7-b), the numerical model underestimates the force level at the end of the initial branch with respect to the experimental response, where the first peak is consistently observed above 3.5–4.0 kN. This discrepancy is mainly attributed to the simplified calibration of the interface peak strength, which is derived from averaged bond parameters and does not explicitly account for early-stage effects such as local matrix confinement, initial friction mobilization, and non-uniform stress redistribution along the bonded length. As a result, the present formulation is primarily aimed at capturing the global trends and post-peak mechanisms, rather than providing an exact prediction of the (first) peak force.

It is also worth noting that the plateau-like branch experimentally observed in several anchored tests is only partially reproduced by the present formulation. This is mainly due to modeling the spike through a linear elastic spring, which captures the kinematic constraint and the

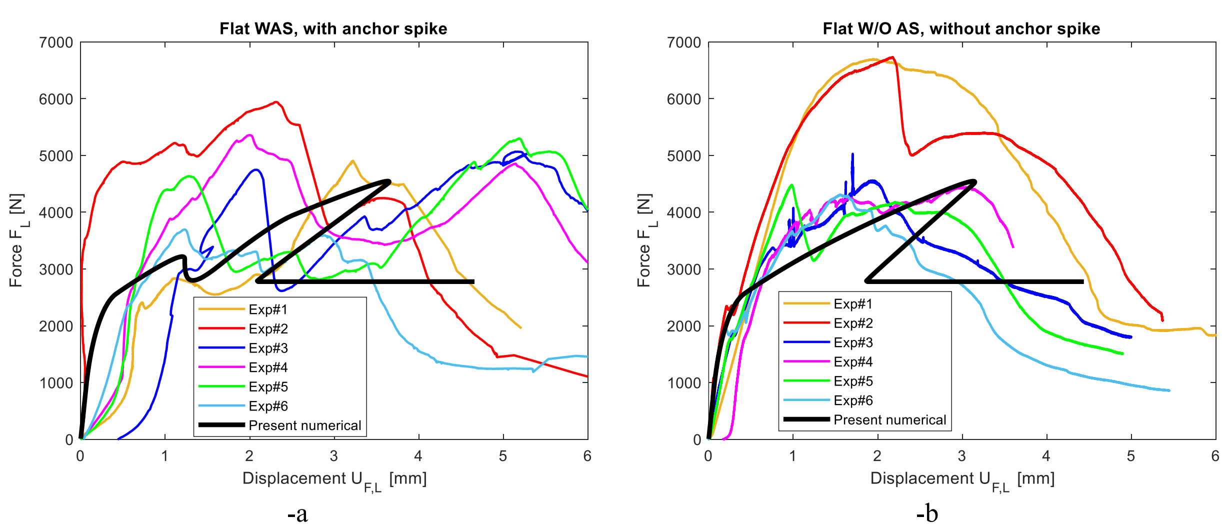

Fig. 7. Flat case. Comparison between numerical global force-displacement curves and experimental data. -a: with anchor spike. -b: without anchor spike.

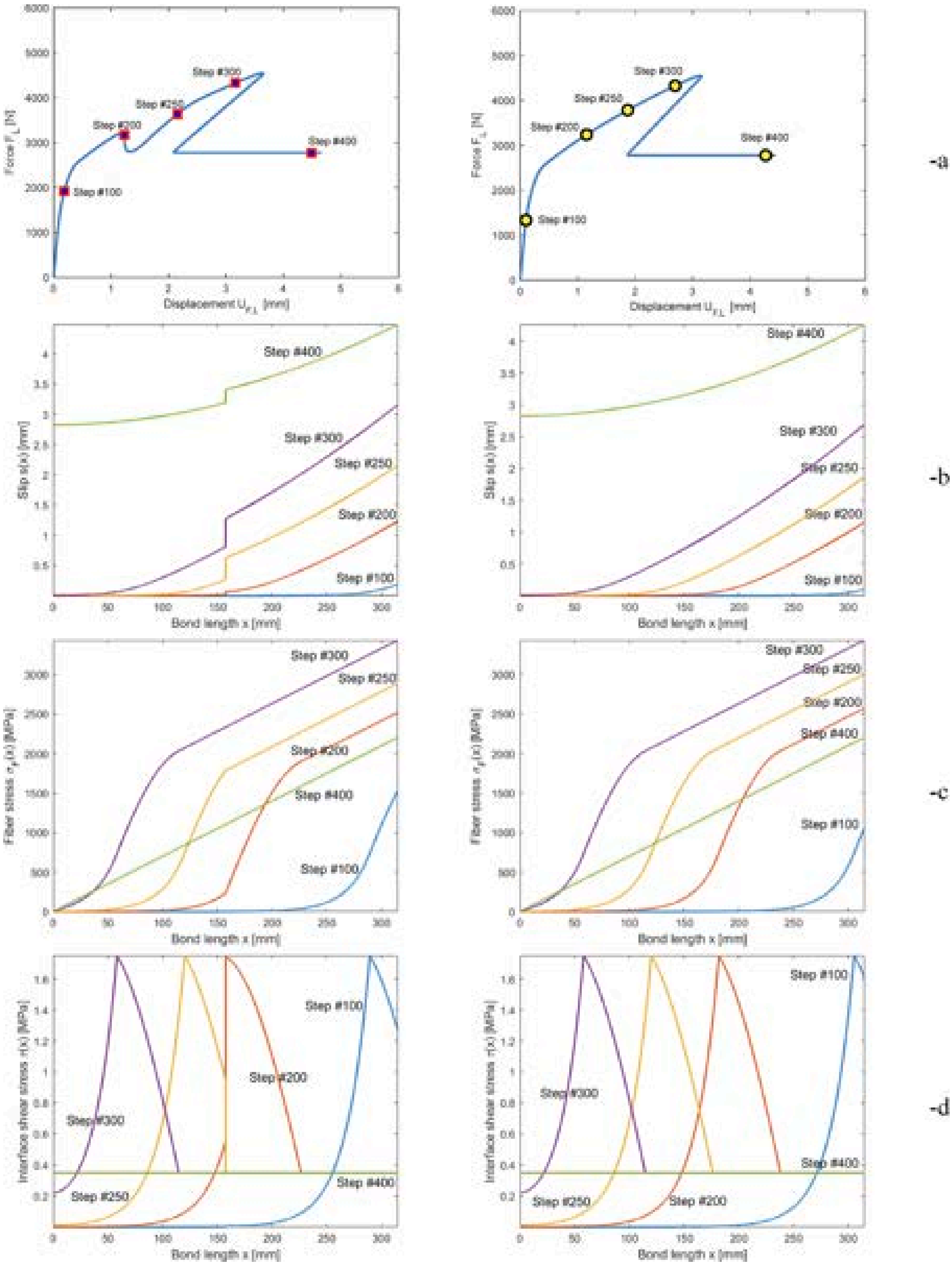

Fig. 8. Flat case, comparison of internal variables along bond length at different simulation steps between the case with (left subfigures) and without (right subfigures) anchor spike. -a: step identification in the global force-displacement curves. -b: slip. -c: fiber layer normal stress. -d: interface shear stress.

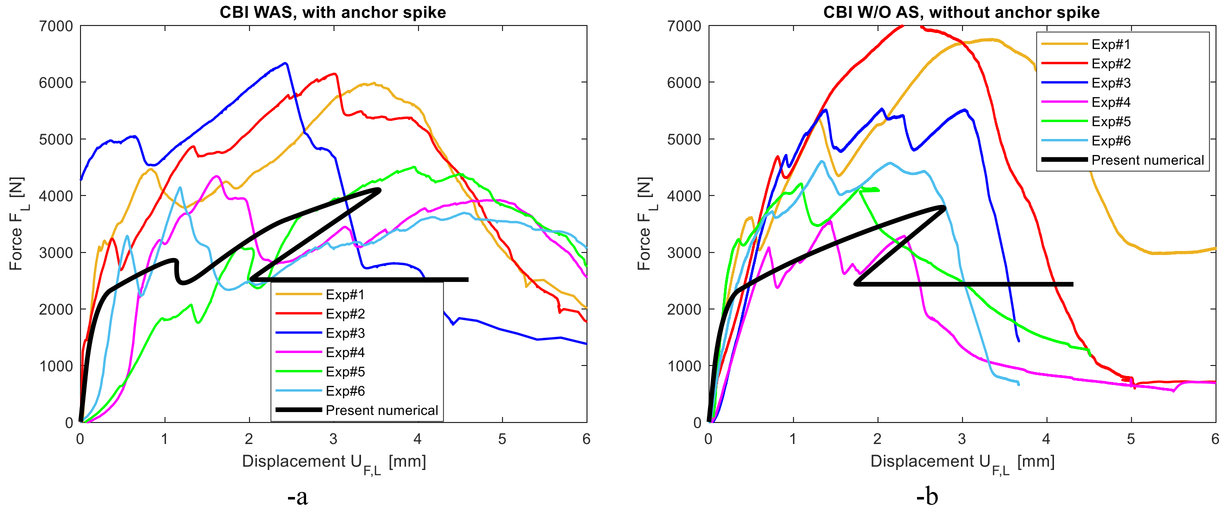

Fig. 9. CBI case. Comparison between numerical global force-displacement curves and experimental data. -a: with anchor spike. -b: without anchor spike.

delayed mobilization of the rear segment, but cannot represent the progressive and dissipative engagement of the anchor system (fan-region cracking, frictional sliding, and gradual activation). Introducing a nonlinear/dissipative spring law would improve the plateau prediction, but it would also increase the number of parameters to set, reducing the "ready-to-use" nature of the present low-dimensional model.

Plotting local quantities (see Fig. 8) helps to understand, in greater detail, the differences between the two cases throughout the loading process. Specifically, in Fig. 8, for five selected analysis steps identified on the global curves by red squares and yellow circles for specimens with and without the spike, respectively, the slip variable, fiber normal stress, and interface shear stress are plotted along the bond length. The subfigures on the left refer to the case with the spike, while the subfigures on the right pertain to the pillars without the spike.

Two important features stand out: (i) the slip jump at the spike and (ii) the different propagation patterns of the debonding front in the two configurations, as shown by the $\tau(x)$ distributions. At Step #200, when the right segment is fully de-bonded, and the left segment starts to carry load, the spike smooths the local shear-stress peaks near x_s. The unloaded segment then mobilizes progressively until it reaches its own peak strength. After that, the $\tau(x)$ profile gradually converges to the shape observed without the spike (yellow curves in Fig. 8-d).

An additional point concerns the normal stress σ_n. In this model, σ_n is proportional to the fiber axial stress σ_F; in the flat case $\sigma_n = 0$ because $R_c \rightarrow \infty$. Near the free edge, σ_F is constrained to vanish, so σ_n remains small over a long portion of the bonded length, regardless of curvature. Therefore, using for the unloaded segment an interface law that does not depend on σ_n (Fig. 6-a) introduces only a negligible error and supports the assumption stated at the beginning of this section.

Similar considerations can be repeated for the CBI case (low curvature). In Fig. 9, the numerical force-displacement curves are compared with experimental outcomes, in the presence (Fig. 9-a) and absence (Fig. 9-b) of an anchor spike. In both cases, the numerical force–displacement curves fall within the experimental scatter.

Although experiments 1–3 and 4–6 correspond to two different spike turning-up procedures, no systematic clustering of the responses can be identified. The apparent differences between subsets fall within the experimental scatter and are mainly attributed to installation-related variability rather than to the turning-up configuration itself. For this reason, a single equivalent interface model was adopted.

It should be noted that the present formulation tends to underestimate the force level at the end of the initial branch and, in some cases, the peak load. This behavior is not primarily related to calibration inaccuracies, but rather to the intrinsic simplifications of the model, which adopts an equivalent interface law calibrated on averaged parameters and intentionally neglects early-stage local effects such as progressive matrix confinement, initial friction mobilization, and non-uniform stress redistribution along the bonded length. As a result, the model is primarily intended to capture the dominant global trends and post-peak mechanisms, rather than providing an exact prediction of the first peak force.

With the spike, the response shows a two-stage pattern: after the first peak and a short drop, the rear bonded length is mobilized, and the ultimate slip increases. The change in peak load is small. Without the spike, debonding propagates monotonically from the loaded edge, and the ductility is lower. The snap-back segments predicted by the model correspond to force-control instability and cannot be followed in experimental displacement-controlled tests. For this reason, the comparison with experimental results refers to the stable equilibrium path only, which is the physically accessible response under the adopted testing protocol.

Fig. 10 shows the profiles along the bonded length for the CBI case at five representative load steps. With the spike (left column), the anchor acts as a barrier: once the loaded segment is fully de-bonded, the debonding front is arrested at x_s, local shear $\tau(x)$ near the spike drops, and the rear segment is mobilized with delay. A slip jump is evident at x_s, while axial force in the reinforcement remains continuous across the spike, consistent with the spring model. The normal stress σ_n on the loaded segment stabilizes at about 0.04 MPa, then rapidly decays to near zero beyond the spike toward the free edge. Without the spike (right column), the debonding front propagates smoothly from the loaded edge to the free edge, with no slip discontinuity and a monotonic decay of both $\tau(x)$ and $\sigma_n(x)$. These local patterns explain the two-stage global response and the moderate increase in ultimate slip observed with the spike.

Finally, Fig. 11 and Fig. 12 summarize the results obtained for CAI specimens (pillars with high curvature).

Similarly to what was observed for Fig. 9, the numerical response in Fig. 11 tends to underestimate the force level at the end of the initial branch and, in some cases, the peak load. This behavior is attributed to the simplified nature of the model and to the use of averaged interface parameters, which neglect early-stage local effects and aim at capturing global trends rather than specimen-specific peak values.

Having a look at the global response of the model, again, the agreement with experimental evidence is considered satisfactory in terms of global trends and failure mechanisms, despite some

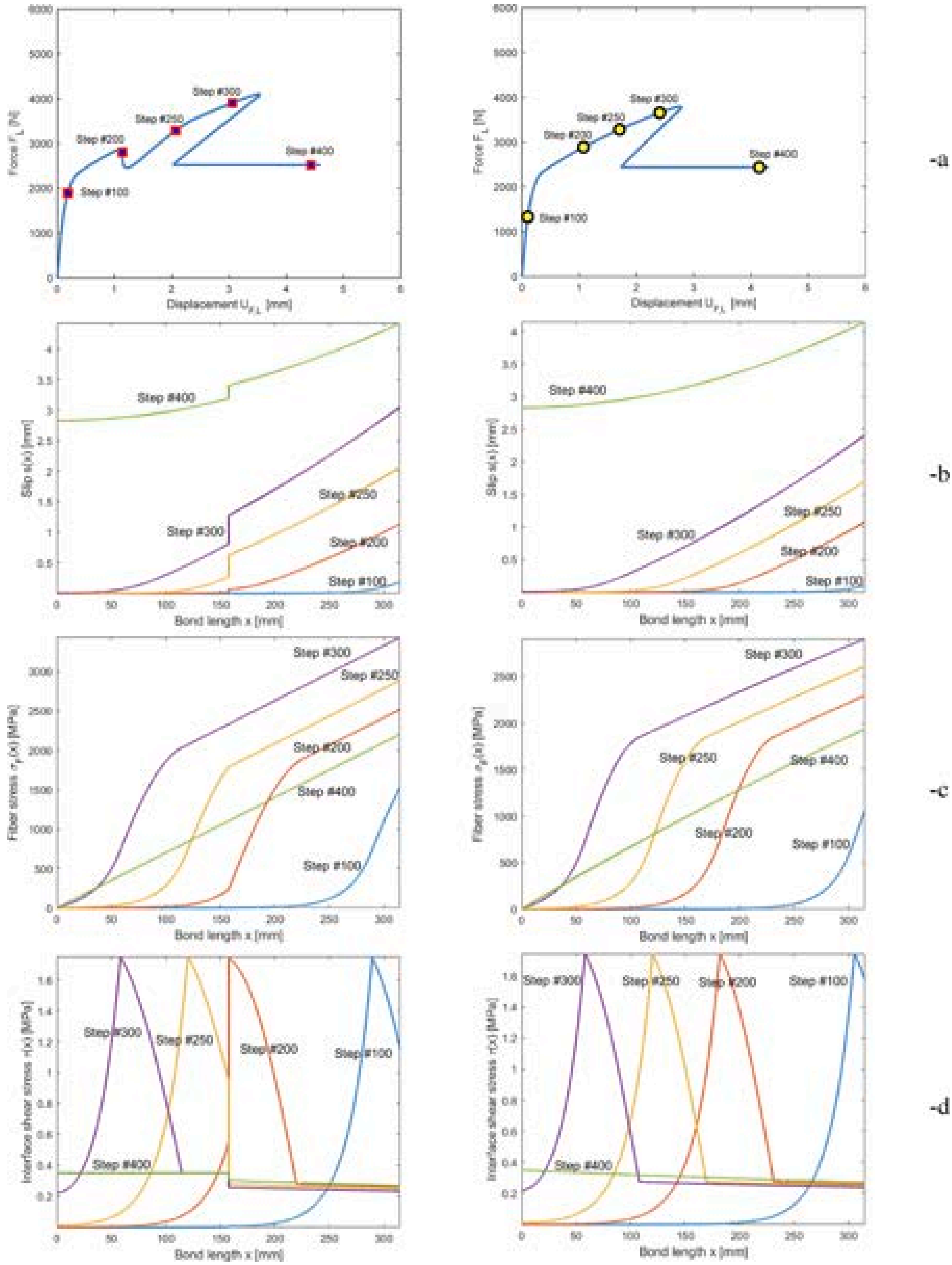

Fig. 10. CBI case, comparison of internal variables along bond length at different simulation steps between the case with (left subfigures) and without (right subfigures) anchor spike. -a: step identification in the global force-displacement curves. -b: slip. -c: fiber layer normal stress. -d: interface shear stress.

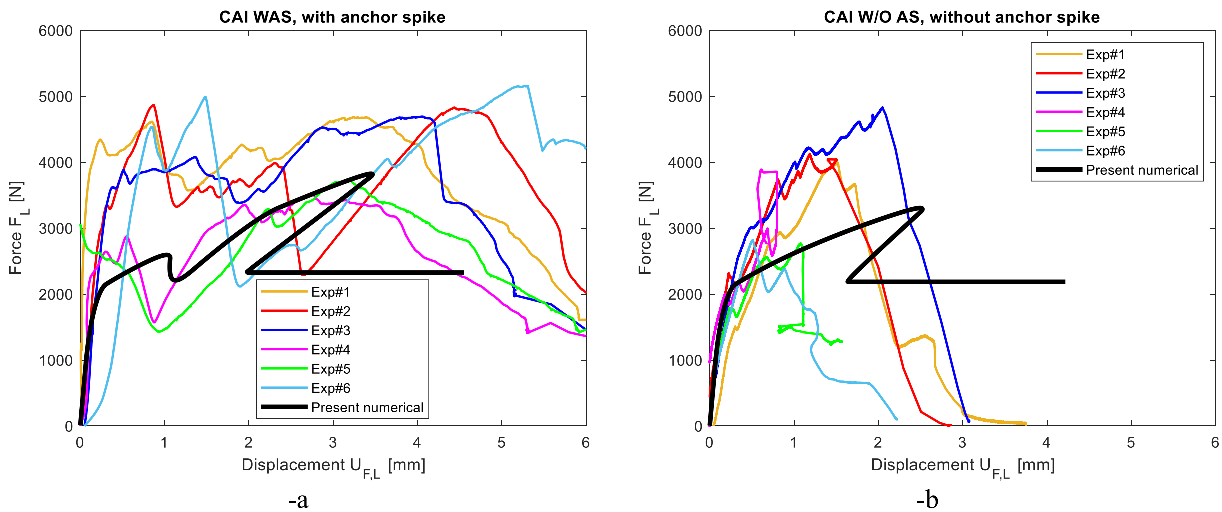

Fig. 11. CAI case. Comparison between numerical global force-displacement curves and experimental data. -a: with anchor spike. -b: without anchor spike.

discrepancies in peak load and post-peak transition details. Globally and locally, the spike acts in the same way as observed for the flat and low-curvature cases. Normal stresses are higher, stabilizing to values near 0.09–0.10 MPa in the loaded part of the reinforcement, and reducing both the ultimate ductility and the carried peak load, consistent with the frictional behavior assumed for the interface.

However, it is worth mentioning that the present numerical model is meant to prioritize simplicity, since all nonlinearity is lumped at a fictitious interface between elastic reinforcement and rigid support. Consequently, and unavoidably, in line also with existing literature adopting similar approaches (such as rigid with softening and residual strength [52], bilinear with softening [53,54], or non-linear with softening, C^1 discontinuous [55] or continuous [56,57], it turns out to deviate -sometimes considerably- from the actual experimental behavior.

One may also argue that the behavior of the interface between reinforcement and substrate should be identical between left (free edge) and right parts (loaded edge). When this latter hypothesis is assumed, the results summarized in Fig. 13 are obtained for the CAI case. In particular, Fig. 13-a compares the obtained numerical results with experimental data, whereas Fig. 13-b depicts an “internal” comparison between the phenomenological model when the constitutive behavior of the left part is assumed either in agreement with Table 2 or identical to that of the right part. As it is possible to notice, experimental data fitting loses accuracy in predicting the improvement obtained in both load carrying capacity and ultimate displacement reached, thus aligning less with the primary aim of any phenomenological approach, i.e. to reproduce globally the expected behavior without providing specific micro-mechanical information, as discussed earlier.

No matter about the constitutive law adopted for the interfaces, observing the shape of the global curve obtainable numerically, it is worth noting that it is always characterized by a linear elastic range followed by a pseudo-elastic stage, which, in the presence of the spike, is prolonged after an intermediate drop of the load-carrying capacity suggestive of a full debonding of the right part. The ultimate slip is always followed by a considerable drop in loading, which is rarely observed in experiments.

On the other hand, laboratory data are characterized by large scatter, which is unavoidable, especially in the presence of anchor spikes, and which is a consequence of the imperfect preparation of samples constituted by different materials exhibiting softening. This further complicates the actual stress transfer from FRCM to substrate and stress redistribution, especially in correspondence with the spike. 3D effects are also disregarded, another important feature that limits even more the predictive capabilities of local physical phenomena occurring. This notwithstanding, a quantitative comparison between numerical evidence and experimental results remains interesting.

In particular, in [44], the force–slip curves obtained experimentally in the presence and absence of anchor spikes were post-processed and approximated by an equivalent trilinear law, defining the following three parameters, see also Fig. 14, namely F_{max}, the initial stiffness K_1, and μ_k.

F_{max} and $U_{Fmax,L}$ are the maximum force reached in the force-slip curve and the corresponding displacement, respectively; K_1 is the slope of the first (quasi-)linear branch; $U_{F,L,u}$ is the displacement corresponding to a load drop of 50% of the maximum load. The trilinear diagram is such that the slope of the first branch (segment I) is equal to K_1; the second branch (segment II) ends to the point $\left(U_{Fmax,L}, F_{max}\right)$ and connects to segment I with a slope such that the area under the equilibrium path in the pre-peak phase -from the origin to $\left(U_{Fmax,L}, F_{max}\right)$- is equal to the area under segments I–II of the trilinear curve, thereby identifying the slip $U_{F,L,e}$. μ_k is defined as $\mu_k = U_{Fmax,L}/U_{F,L,e}$, and it can be regarded as an indirect measure of the energy dissipation capacity.

The third branch of the trilinear curve (segment III) extends from $\left(U_{Fmax,L}, F_{max}\right)$ to the ultimate slip value $U_{F,L,u}$ and its slope is such that the area under the equilibrium path in the post-peak phase equals the area under segment III of the equivalent trilinear curve.

The same parameters can be calculated for numerical curves, and a quantitative synoptical comparison with experimental data is provided in Fig. 15 for all curvatures.

From a detailed analysis of the results obtained, the following considerations hold:

- Numerical elastic stiffness K_1 does not change with the introduction of the anchor spike, in agreement with experimental observations. The numerical model overestimates K_1, because of the simplifying hypotheses made (for instance, a rigid support is assumed).
- μ_k is systematically higher for a twofold reason, namely because K_1 is larger in the numerical model and $U_{Fmax,L}$ is on average similar. It is more interesting to observe that, in both the experiments and the numerical model μ_k increases with the introduction of the spike, with the same trend and with similar proportions.
- Peak load does not present substantial variations when a spike is present, an outcome fairly in agreement with the mean values

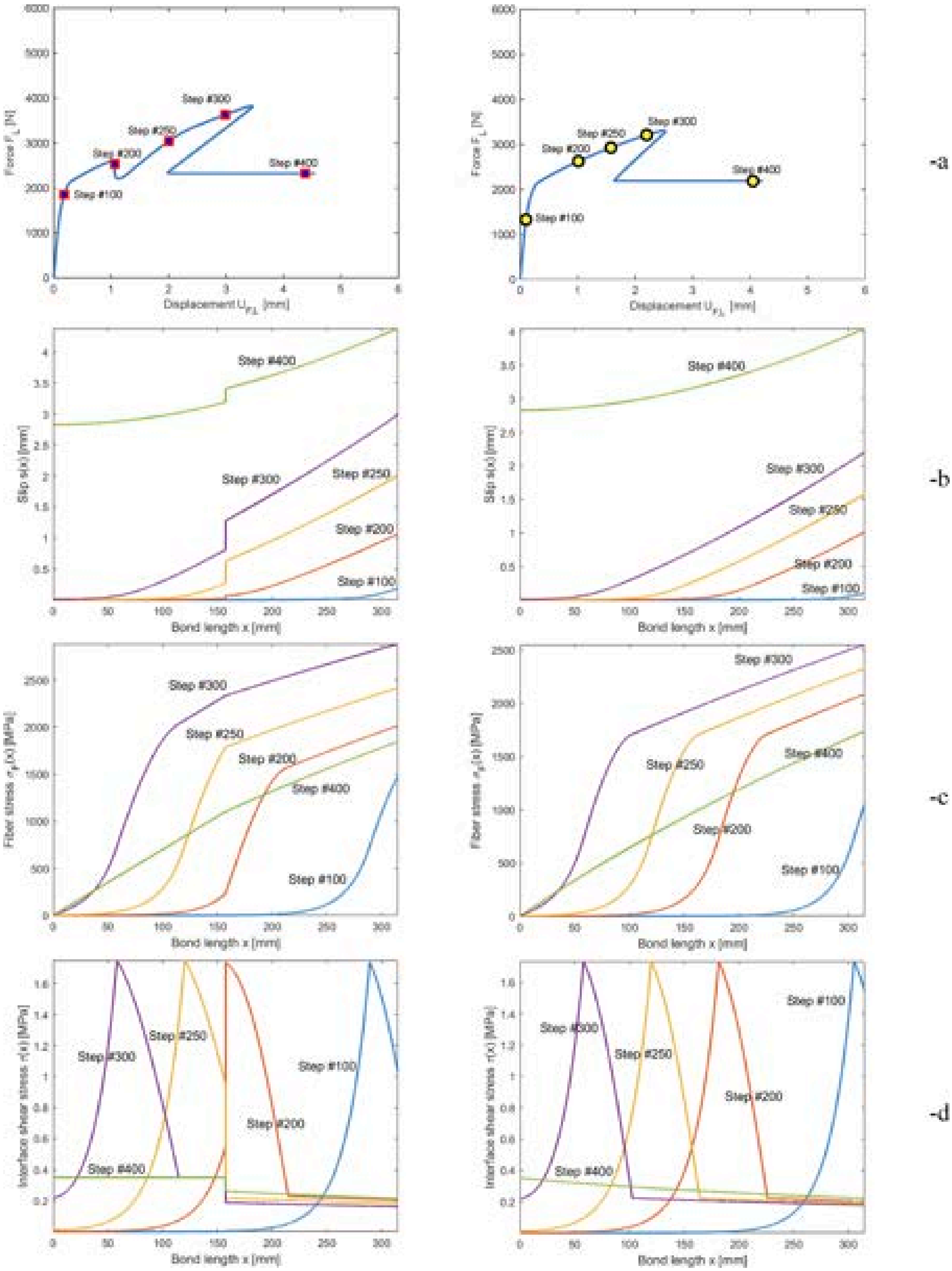

Fig. 12. CAI case, comparison of internal variables along bond length at different simulation steps between the case with (left subfigures) and without (right subfigures) anchor spike. -a: step identification in the global force-displacement curves. -b: slip. -c: fiber layer normal stress. -d: interface shear stress.

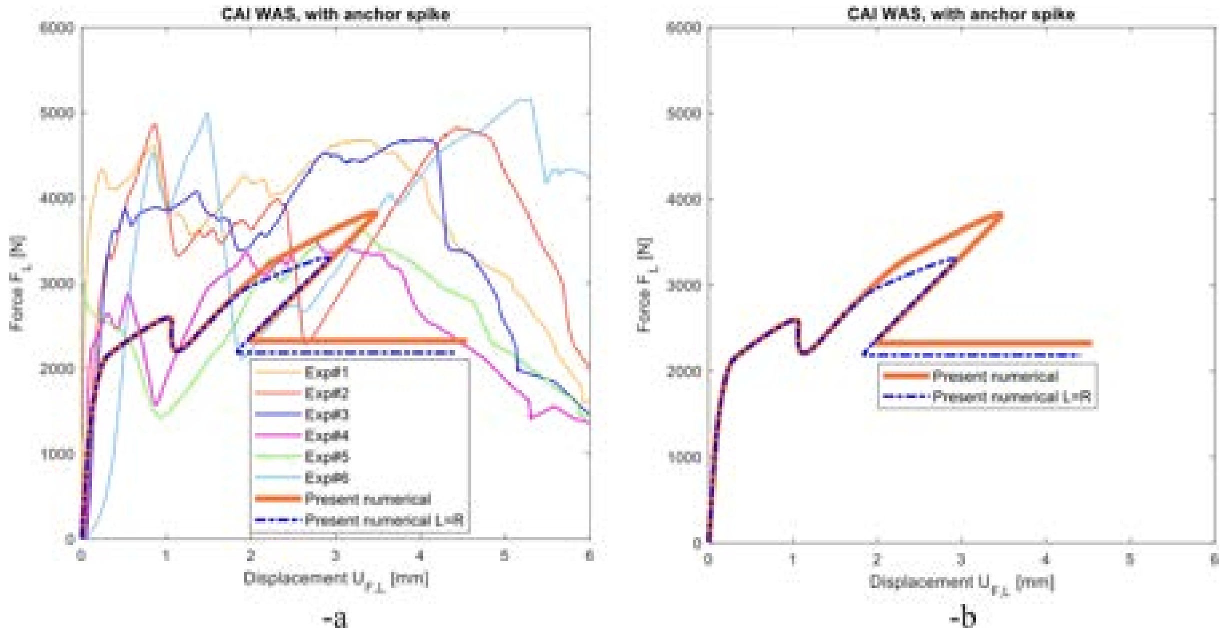

Fig. 13. CAI WAS case, comparison between the numerical response obtained with Left L and Right R mechanical properties of the interface as in Table 2 ("Present numerical") and with Left L and Right R mechanical properties identical and equal to the right part ("Present numerical L=R"). -a: comparison with experimental data. -b: internal comparison between the two numerical models.

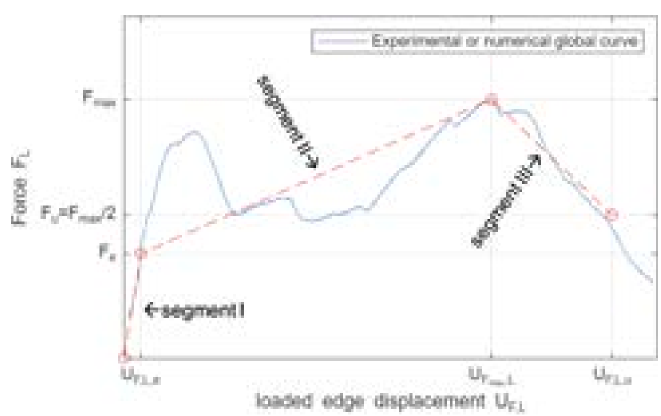

Fig. 14. Deduction of F_e, F_{max}, $U_{F,L,e}$, $U_{F,L,u}$, $U_{F_{max},L}$ from experimental or numerical global $U_{F,L}$-F_L curves.

observed experimentally, even if the large scatter exhibited by experimental data should be considered.

From an overall analysis of the comparisons carried out considering the overly simplistic assumptions made for the proposed model (intended for practical use), the agreement with experimental data may still be considered satisfactory, confirming that useful predictions of the expected global behavior may be made without the need to perform costly experimental campaigns.

Fig. 16 and Fig. 17 compare -as far as numerical results are concerned- Flat, CBI, and CAI configurations, each with and without a spike, to isolate the curvature effect. Three main aspects are worth noting. First, in the Flat case, the spike does not increase the peak load and raises only slightly the ultimate slip, although the two-stage post-peak response is evident.

Second, in CBI, the spike delays the debonding front progression and produces a clearer two-stage response, with a moderate gain in the energy dissipation capacity and only minor changes in peak load. It should be clarified that the two-stage response does not necessarily correspond to two distinct peaks in the global force–displacement curve. Rather, it reflects a transition between two different load transfer mechanisms, which in flat and low-curvature specimens may appear as a change in softening slope or a mild plateau and can be partially masked by experimental scatter. A clearly distinguishable two-stage response at the global level emerges mainly in the CAI configuration, where curvature-induced normal stresses amplify the effect of the spike.

Third, in CAI, the curvature in general reduces both peak load and energy dissipation capacity: the spike still improves the post-peak response and ultimate slip, but the gain remains limited.

It should be noted that, in the absence of spike anchors, the effect of curvature on peak strength is not clearly distinguishable between the Flat and CBI configurations. This is due to the relatively low curvature of the CBI specimens, which induces normal stresses comparable to the experimental scatter and mainly affects the post-peak response rather than the maximum load. A clear detrimental effect on peak strength becomes evident only for the CAI configuration, characterized by higher curvature-induced normal stresses.

Moreover, the comparable peak forces observed in the CAI configuration with and without a spike should be interpreted as a partial mitigation of the curvature-induced strength reduction, rather than as a direct strengthening effect of the anchor.

Quantitatively, the ultimate slip increases in all cases when the spike

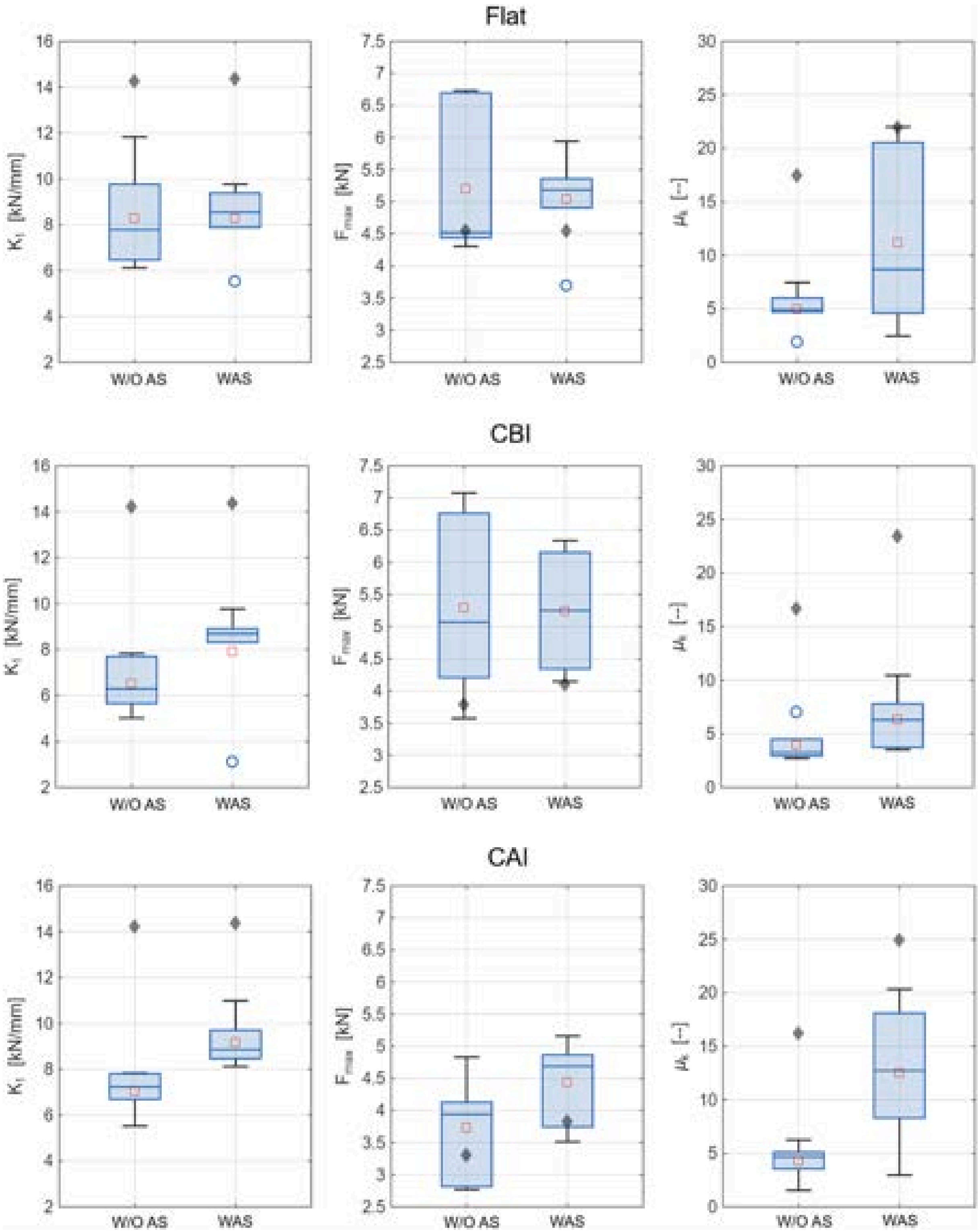

Fig. 15. Quantitative comparison between numerical and experimental data. In each light blue box, the central horizontal segment indicates the median, the bottom and top edges of the box indicate the 25th and 75th percentiles, respectively. The whiskers extend to the most extreme data points, not considering outliers. The mean values within each series are plotted using the "□" symbol. Gray diamonds "◊" refer to the numerical results. Hollow blue circles "o" indicate outliers.

is present, with percentage gains of 15.6% (Flat), 27.1% (CBI), and 36.9% (CAI), in line with the tests. Peak load shows a slight positive change only for curved specimens, with increases of 8.2% (CBI) and 16.6% (CAI). This trend reflects the spike's role in mitigating the adverse effect of positive σ_n at the interface, as captured by the model. In summary, anchors provide little benefit for flat configurations. For intrados reinforcement on arches, the benefit is moderate and becomes more visible as curvature increases.

5. Conclusions

A simplified numerical model suitable for the prediction of the

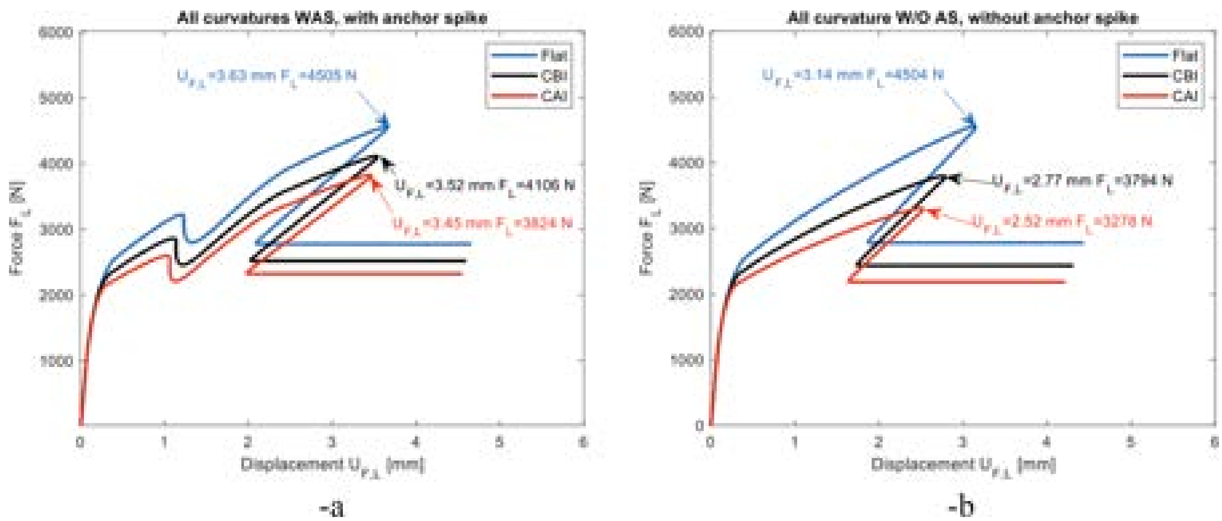

Fig. 16. All curvatures tested. Global force-displacement curves obtained with the model proposed in the presence (-a) and in the absence (-b) of an anchor spike.

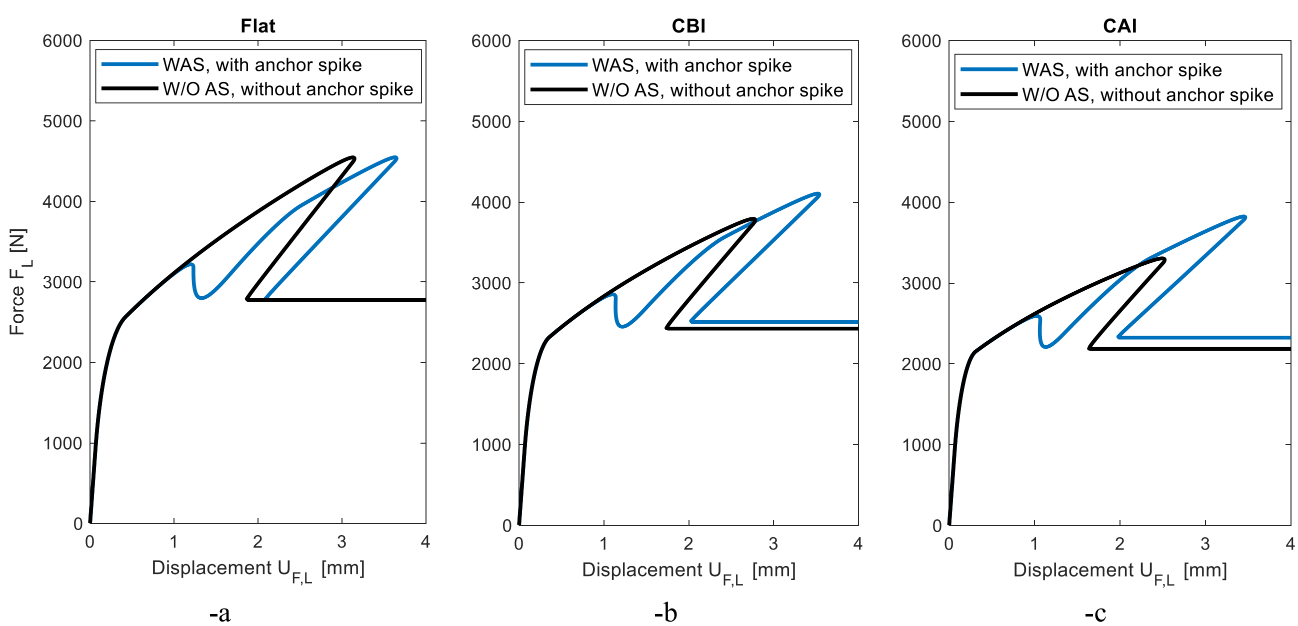

Fig. 17. Comparison between global behavior obtained in the presence and absence of an anchor spike. -a: Flat. -b: CBI. -c: CAI.

behavior of curved masonry pillars reinforced with FRCM strips in the presence of anchor spikes and subjected to single lap shear tests has been presented.

This model follows a simplified approach. All non-linear behavior is lumped into a single equivalent interface between a rigid substrate and a linearly elastic reinforcement idealized as a uniaxial layer with equivalent thickness.

The presence of the spike has been considered, introducing a linear elastic spring which connects the unloaded and loaded portions of the reinforcement, where conventionally the term “left” (L) has been used to indicate FRCM located between the free edge and spike, and the term “right” (R) the rest. The derived field equation is standard and has led to writing a second-order non-linear differential equation in the independent variable of slip. Since the support has been assumed rigid, the slip has turned out to coincide with the axial displacement of the fiber. The only difference with the specimens without a spike is that the latter has been modeled by means of a linear spring connecting the left and right parts. Numerically, the problem has been tackled explicitly, converting a BVP into a Cauchy’s problem, the latter solved by making use of a standard Runge-Kutta RK4 in-house developed kernel. Conversion has been possible by transferring the boundary condition applied at the loaded edge (a prescribed displacement/slip) to the free one. Two Cauchy’s problems have been solved in series, starting from the free edge, deducing slip and fiber tensile stress in correspondence of the spike, transferring such results as initial conditions for the right part, and finally solving the second Cauchy’s problem numerically. To validate the numerical results obtained, a wide comparison with an experimental program conducted by the authors on curved pillars reinforced with FRCM and equipped with a central spike has been carried out. The reasonably good agreement with experimental outcomes -considering the unavoidable approximations introduced- confirms the predictive capabilities of the simple model proposed. In particular, the results highlight that curvature generally reduces both peak load and energy dissipation capacity. However, in the presence of spike anchors, the relative post-peak benefit provided by the spike anchor in terms of ultimate slip becomes more evident as curvature increases, without implying an intrinsic energy dissipation enhancement associated with curvature itself.

In this context, “common practitioners” refers to structural engineers familiar with simplified mechanical modeling and basic numerical tools, for whom the proposed low-dimensional and fully explicit formulation can be implemented in straightforward computational environments and used as a support tool for preliminary assessment, parametric analyses, and interpretation of experimental evidence, rather than as a direct design-by-formula approach. On the other hand, it is worth mentioning that specific existing literature is -to the best of the authors’ knowledge- still insufficient.

It should be emphasized that the model is not intended to reproduce all local response features in a pointwise manner, but rather to provide a simplified mechanical interpretation of the dominant trends observed experimentally, particularly concerning the role of curvature and spike anchors.

Although the unstable snap-back branches predicted numerically are not directly observable in displacement-controlled experimental tests, they provide valuable information on the softening behavior of the interface and on the associated energy dissipation capacity under extreme loading scenarios, such as strong seismic actions.

In particular, the proposed formulation should be interpreted as a reduced-order mechanical representation aimed at capturing global trends rather than local damage evolution. Its applicability is therefore limited to configurations where the debonding process is predominantly governed by interface mechanisms, while complex three-dimensional effects are not explicitly resolved.

Future work will focus on improvements of the numerical approach for the following key issues:

- It appears crucial to find a reliable experimental strategy to directly estimate the stiffness value K_s to adopt for the anchor spike, instead of using the numerical tuning here proposed.
- Considering that masonry is constituted by the assemblage of bricks and mortar, and that historical brickwork is often highly irregular, the use of continuous interface parameters represents an intrinsic limitation of the proposed approach, as it cannot fully capture local heterogeneity and discontinuities affecting bond behavior. This limitation may be mitigated in future developments by adopting spatially varying interface properties, distinguishing regions in contact with mortar joints or blocks, introducing damageable substrate models, and accounting for the stochastic nature of interface mechanical properties.
- A more sophisticated approach would be preferable to have a better insight into the mechanical role played by the spike. The most attractive option seems to avoid the concentration of all non-linearity on a fictitious interface between elastic reinforcement and rigid substrate, distinguishing all three layers of the reinforcement, assuming the matrix as elasto-brittle, PBO bundles linear elastic, and using non-linear interfaces between them, similarly to what was done in [38]. It appears also mandatory to explicitly model the spike, especially the fanning system on the loaded side, for instance, by the introduction of an additional layer.
- As far as the practical implications are concerned, it appears interesting to study different geometric configurations, for instance, with a single spike installed in a different position, e.g., either nearer the loaded or the free edge, or in the presence of more than one spike. In perspective, the simplified modeling approach used here may be useful to guide future experimentation towards the most effective configuration (and number) of spikes to install.

Declaration of competing interest

The authors declare that they have no known competing financial interests or personal relationships that could have appeared to influence the work reported in this paper.

Appendix A. Spike stiffness K_S tuning

The evaluation of the equivalent stiffness K_s of the spike is crucial for the predictivity of the model proposed, but its direct experimental derivation is tricky.

In order to cope with such an issue, an indirect estimation is possible, ensuring that the global response of the model (force-displacement curve) exhibits the first peak of the load at a pre-established point. In correspondence with it, the loaded R part is almost totally debonded. According to Fig. A.1, such a portion of reinforcement is therefore assumed completely in phases II and III, whereas the unloaded part L is still not mobilized, and hence it is assumed in the elastic stage (phase I).

The analytical solution for the unloaded part (phase I, elastic) is the following:

$$\begin{cases} s_I(x) = C_1^I e^{-\alpha x} + C_2^I e^{\alpha x} \\ \sigma_F(x) = -E_F \alpha C_1^I e^{-\alpha x} + E_F \alpha C_2^I e^{\alpha x} \end{cases} \tag{A1}$$

where $\alpha = \sqrt{\frac{K_I}{E_F t_F}}$ and $K_I = \frac{\tau_{L,0M}}{s_{L,0e}}$.

Eq. (A1) integration constants C_1^I and C_2^I can be determined easily in closed form applying at the free edge a slip $s_I(0) = \bar{s}_{I0}$, which adds to the condition $\sigma_F(0) = 0$, yielding the following solution:

$$C_1^I = C_2^I = \frac{\bar{s}_{I0}}{2} \tag{A2}$$

Considering that the unloaded part is assumed always in stage I, Eq. (A2) allows us to bound the values of slip to apply at the free edge. In particular:

$$0 < \bar{s}_{I0} < \frac{2 s_{L,0e}}{e^{-\alpha \frac{L_b}{2}} + e^{\alpha \frac{L_b}{2}}} \tag{A3}$$

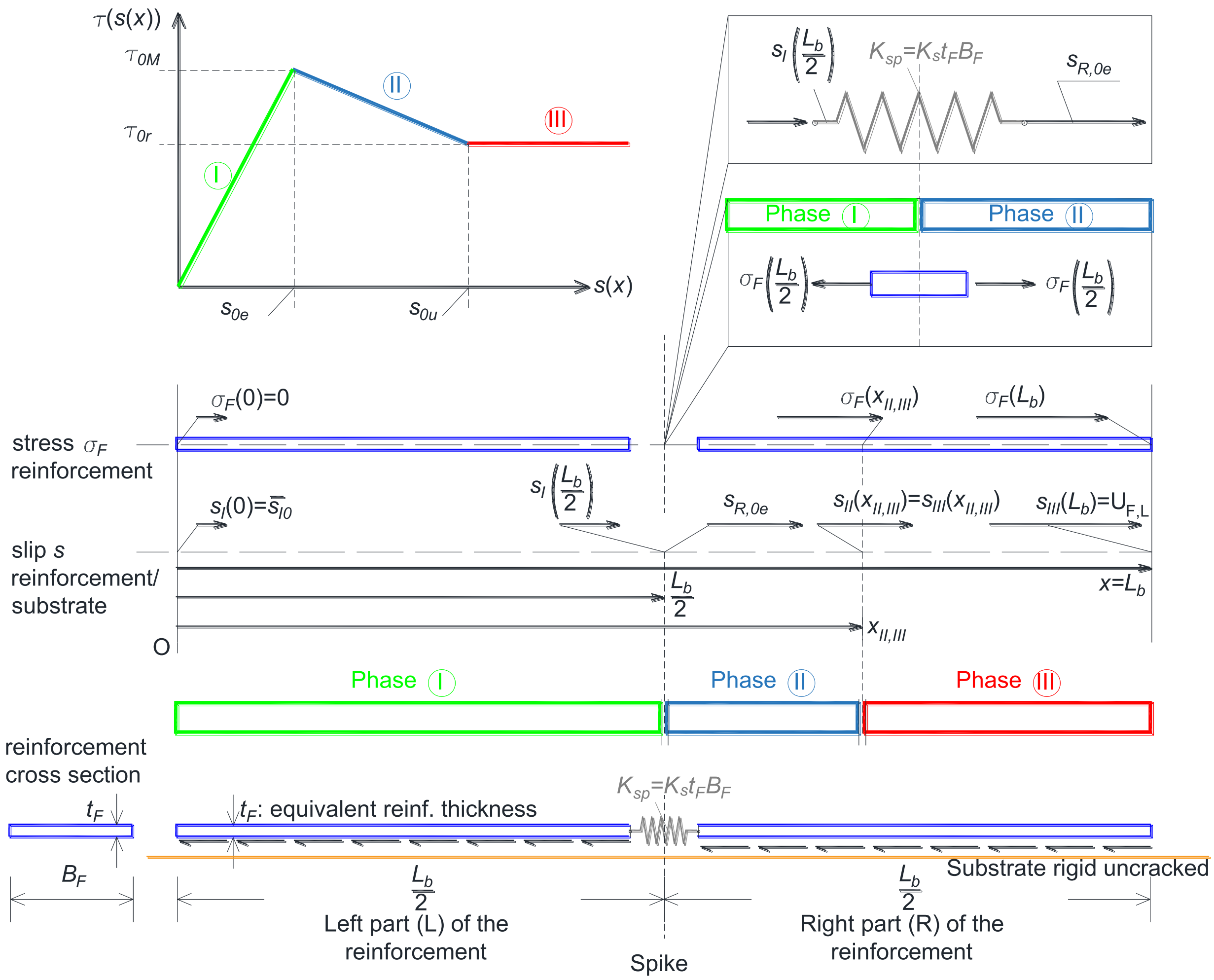

Fig. A.1. Schematic explanation of the procedure followed to tune spike stiffness K_s.

As far as the loaded part is concerned, we assume that the edge in correspondence of the spike exhibits a slip equal to the elastic limit ($s_{R,0e}$), whereas by equilibrium the stress in the fiber is equal to that of the unloaded part. The initial conditions to apply are therefore the following:

$$\begin{cases} s_{II}^{s} = s_{II}\left(\dfrac{L_b}{2}\right) = s_{R,0e} \\ \sigma_F^{s} = \sigma_F\left(\dfrac{L_b}{2}\right) = E_F\alpha\dfrac{\bar{s}_{I0}}{2}\left(-e^{-\alpha\frac{L_b}{2}} + e^{\alpha\frac{L_b}{2}}\right) \end{cases} \tag{A4}$$

According to Eq. (A 4), it is interesting to notice that the value of K_s that produces a slip of the loaded part equal to $s_{R,0e}$ in correspondence of $x = L_b/2$, when at the free edge a slip equal to $\bar{s}_{I0}$ is applied, is the following:

$$\begin{cases} K_s = \dfrac{\sigma_F^{s}}{s_{R,0e} - s_I\left(\dfrac{L_b}{2}\right)} \\ s_I\left(\dfrac{L_b}{2}\right) = \dfrac{\bar{s}_{I0}}{2}\left(e^{-\alpha\frac{L_b}{2}} + e^{\alpha\frac{L_b}{2}}\right) \end{cases} \tag{A5}$$

In the first portion of the loaded part, the interface is all in phase II, so the field equation to solve is the following:

$$\frac{d^2 s_{II}}{dx^2} + \frac{1}{E_F t_F}\frac{\tau_{R,0M} - \tau_{R,0r}}{s_{R,0u} - s_{R,0e}} s_{II} = \frac{1}{E_F t_F}\frac{\tau_{R,0M}s_{R,0u} - \tau_{R,0r}s_{R,0e}}{s_{R,0u} - s_{R,0e}} \tag{A6}$$

Eq. (A6) is a second-order, linear, and non-homogeneous differential equation that admits a closed form solution. In particular, let us define the following constant parameters:

$$\beta=\sqrt{\frac{1}{E_Ft_F}\frac{\tau_{R,0M}-\tau_{R,0r}}{s_{R,0u}-s_{R,0e}}}$$
$$\gamma=\frac{1}{E_Ft_F}\frac{\tau_{R,0M}s_{R,0u}-\tau_{R,0r}s_{R,0e}}{s_{R,0u}-s_{R,0e}} \tag{A7}$$

Substituting Eq. (A7) in Eq. (A6), the closed-form solution of Eq. (A6) is the following:

$$\begin{cases} s_{II}(x)=C_1^{II}cos\beta x+C_2^{II}sin\beta x+\dfrac{\gamma}{\beta^2}\\ \sigma_F(x)=-E_F\beta C_1^{II}sin\beta x+E_F\beta C_2^{II}cos\beta x\end{cases} \tag{A8}$$

where C_1^{II} and C_2^{II} are integration constants that can be derived analytically using Eq. (A4):

$$C_1^{II}=-\frac{E_F\gamma cos\dfrac{\beta L_b}{2}+\sigma_F^s\beta sin\dfrac{\beta L_b}{2}-E_F\beta^2 s_{R,0e}cos\dfrac{\beta L_b}{2}}{E_F\beta^2}$$
$$C_2^{II}=\frac{-E_F\gamma sin\dfrac{\beta L_b}{2}+\sigma_F^s\beta cos\dfrac{\beta L_b}{2}+E_F\beta^2 s_{R,0e}sin\dfrac{\beta L_b}{2}}{E_F\beta^2} \tag{A9}$$

If the bond length L_b is sufficiently long, in correspondence with the abscissa $x_{II,III}$ ($\frac{L_b}{2}<x_{II,III}\le L_b$), the interface passes from stage II to stage III. $x_{II,III}$ can be found numerically by evaluating the root of the following non-linear equation:

$$C_1^{II}cos\beta x+C_2^{II}sin\beta x+\frac{\gamma}{\beta^2}=s_{R,0u} \tag{A10}$$

Between $x_{II,III}$ and L_b, the field equation can be written as follows:

$$\frac{d^2s_{III}}{dx^2}=\frac{\tau_{R,0r}}{E_Ft_F} \tag{A11}$$

The closed-form solution of Eq. (A11) is the following:

$$\begin{cases} s_{III}(x)=C_1^{III}+C_2^{III}x+\dfrac{1}{2}\dfrac{\tau_{R,0r}}{E_Ft_F}x^2\\ \sigma_F(x)=E_FC_2^{III}+\dfrac{\tau_{R,0r}}{t_F}x\end{cases} \tag{A12}$$

Where C_1^{III} and C_2^{III} integration constants can be derived analytically using (A 12) at $x=x_{II,III}$ and imposing there the continuity of slip and longitudinal stress in the fiber:

$$\begin{cases} s_{II}(x_{II,III})=C_1^{II}cos\beta x_{II,III}+C_2^{II}sin\beta x_{II,III}+\dfrac{\gamma}{\beta^2}=C_1^{III}+C_2^{III}x_{II,III}+\dfrac{1}{2}\dfrac{\tau_{R,0r}}{E_Ft_F}x_{II,III}^2\\ \sigma_F(x_{II,III})=-E_F\beta C_1^{II}sin\beta x_{II,III}+E_F\beta C_2^{II}cos\beta x_{II,III}=E_FC_2^{III}+\dfrac{\tau_{R,0r}}{t_F}x_{II,III}\end{cases} \tag{A13}$$

From Eq. (A13), the explicit expressions for C_1^{III} and C_2^{III} are the following:

$$\begin{cases} C_2^{III}=-\beta C_1^{II}sin\beta x_{II,III}+\beta C_2^{II}cos\beta x_{II,III}-\dfrac{\tau_{R,0r}}{E_Ft_F}x_{II,III}\\ C_1^{III}=C_1^{II}cos\beta x_{II,III}+C_2^{II}sin\beta x_{II,III}+\dfrac{\gamma}{\beta^2}-C_2^{III}x_{II,III}-\dfrac{1}{2}\dfrac{\tau_{R,0r}}{E_Ft_F}x_{II,III}^2\end{cases} \tag{A14}$$

The displacement of the fiber at the loaded edge $U_{F,L}$ and the corresponding applied force F_L are finally computed using again Eq. (A12) and assuming $x=L_b$ once that C_1^{III} and C_2^{III} are known from Eq. (A14):

$$\begin{cases} U_{F,L}=C_1^{III}+C_2^{III}L_b+\dfrac{1}{2}\dfrac{\tau_{R,0r}}{E_Ft_F}L_b^2\\ F_L=E_Ft_FB_F\left(C_2^{III}+\dfrac{\tau_{R,0r}}{E_Ft_F}L_b\right)\end{cases} \tag{A15}$$

With reference to the flat case and the corresponding global experimental data, the abaci of Fig. A.2 can be used. They were produced according to the following kernel:

1) Assign a value for slip $s_I(0)=\bar{s}_{I0}$ within the range $0<\bar{s}_{I0}<\frac{2s_{L,0e}}{e^{-\alpha\frac{L_b}{2}}+e^{\alpha\frac{L_b}{2}}}$;
2) Calculate K_s according to Eq. (A5);
3) Compute C_1^{II} and C_2^{II} according to Eq. (A9);
4) Find numerically $x_{II,III}$, Eq. (A10);
5) Compute C_1^{III} and C_2^{III} according to Eq. (A14);
6) Find the fiber displacement $U_{F,L}$ at the loaded edge and the corresponding applied force F_L using (A15).

Assuming that the experimental first peak (debonding of the loaded part) occurs at a displacement of the loaded edge equal to $s_{III}(L_b)$=$U_{F,L}$=1.23 mm, Fig. A.2 indicates a stiffness $K_s = 4960\frac{N}{mm^3}$, with a corresponding force $F_L = 3174N$.

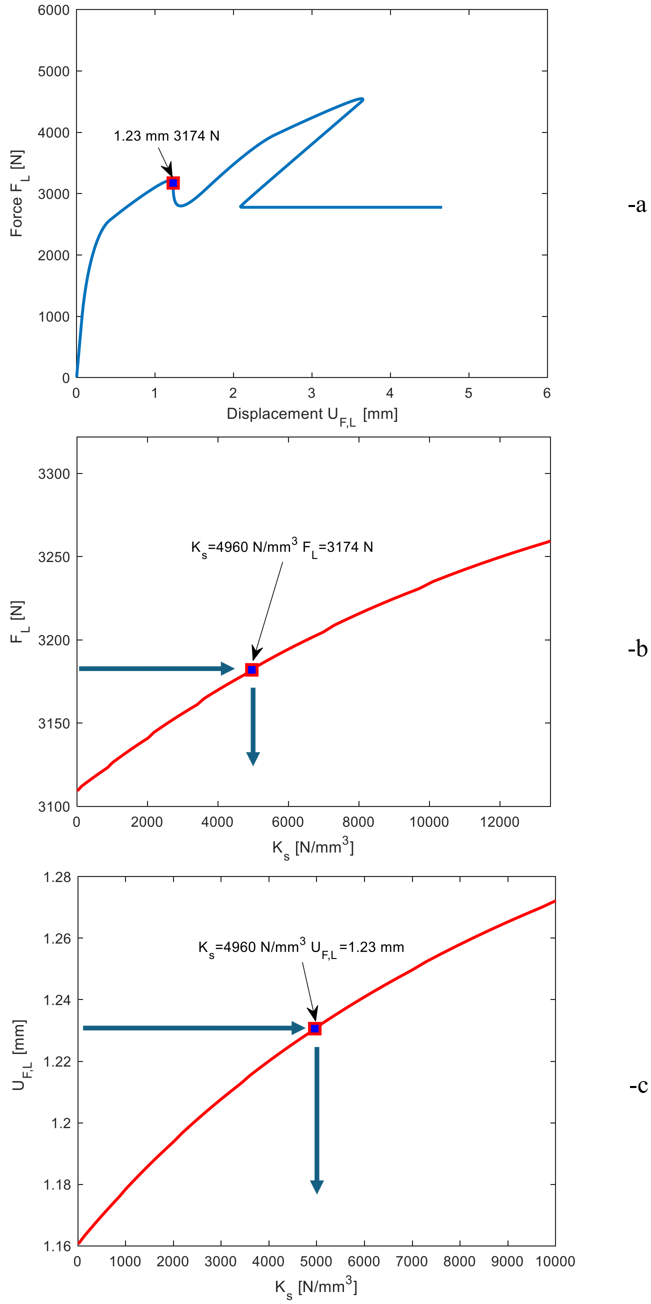

Fig. A.2. Ready-to-use abaci to find when the model will exhibit the first peak load (full delamination of the loaded part), evaluation of K_s. -a: Point selected to tune K_s (from experimental data). -b: K_s-F_L abacus. -c: K_s-$U_{F,L}$ abacus.

The model also allows straightforward sensitivity analyses, carried out to evaluate the role played by the values set in input for the different constants. Fig. A.3 depicts a synopsis of the results obtained by varying K_s (subfigure -a) and the residual strength of the interface $\tau_{L,0r} = \tau_{R,0r} = \tau_{0,r}$ (subfigure -b). As it is possible to notice, the effect of the spike (i.e. of K_s), see Fig. A.3-a, is (i) to increase/decrease the ultimate displacement and (ii) because of the delayed activation of the unloaded part of reinforcement in case of smaller values of K_s, to increase the load carrying drop in correspondence of the full debonding of the right part. On the contrary, the role played by $\tau_{0,r}$ ($K_s = 4960\frac{N}{mm^3}$ in the simulations) is to increase/decrease the slope of the pseudo-linear behavior observed when full debonding activates, hence varying both the peak load carrying capacity and the ultimate displacement, see Fig. A.3-b.

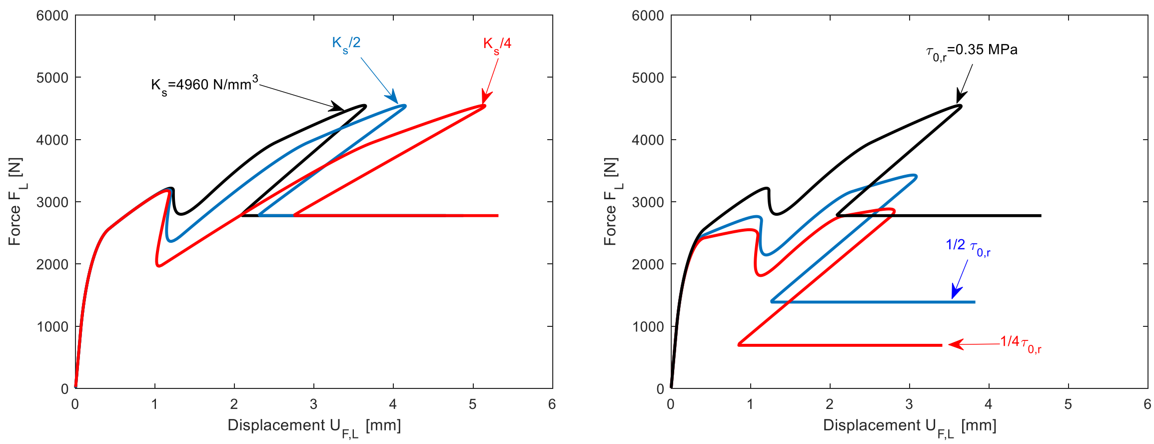

-a -b

Fig. A.3. Sensitivity analysis for the Flat case varying K_s (-a) and $\tau_{0,r}$ (-b).

Appendix B. Boundary value problem (BVP), alternative solution via finite differences

The transfer of the imposed slip from the loaded edge to the free one is not the only numerical procedure that can be adopted. Indeed, with reference to Eqs. (8) and (9), the present debonding problem can be rewritten as a standard BVP as follows (see also Eqs. (14) and (17)):

$$\begin{cases} \dfrac{\mathrm{dy}}{\mathrm{dx}} = \begin{bmatrix} \dfrac{\mathrm{dy}_1}{\mathrm{dx}} \\ \dfrac{\mathrm{dy}_2}{\mathrm{dx}} \end{bmatrix} = \begin{bmatrix} \mathrm{y}_2 \\ \dfrac{\tau(\mathrm{y}_1)}{\mathrm{E_F t_F}} \end{bmatrix} \\ \mathrm{y}_2(0) = 0 \\ \mathrm{y}_1(\mathrm{L_b}) = \mathrm{U_{F,L}} \end{cases} \tag{B1}$$

In Eq. (B1) one may notice that the following change of variables has been made: $y_1 = s$ and $y_2 = \frac{dy_1}{dx}$.

The BV problem (B1) can be tackled by adopting a standard Euler forward finite differences scheme.

Indeed, let us assume a uniform space partitioning along the bonded length, see Fig. B.1, where $(n+1)$ knots are used both for L and R sides, so that the partitioning length h is identical before and after spike location, and kept hence equal to $h = L_b/(2n)$.

For the $(i+1)$ knot, according to Eq. (B1), y_1^{i+1} and y_2^{i+1} can be deduced as follows:

$$\begin{aligned} &\frac{\mathrm{y}_1^{\mathrm{i}+1} - \mathrm{y}_1^{\mathrm{i}}}{\mathrm{h}} = \mathrm{y}_2^{\mathrm{i}} \\ &\frac{\mathrm{y}_2^{\mathrm{i}+1} - \mathrm{y}_2^{\mathrm{i}}}{\mathrm{h}} = \frac{\alpha^{\mathrm{n_I},\mathrm{k}-1}}{\mathrm{E_F t_F}}\mathrm{y}_1^{\mathrm{i}} + \frac{\beta^{\mathrm{n_I},\mathrm{k}-1}}{\mathrm{E_F t_F}} \end{aligned} \tag{B2}$$

where k is the time step (intending with this expression the k-th increment of slip applied at the loaded edge), n_I=I, II, III is the active stage of the interface in correspondence of the i-th knot at time step k-1, and $\alpha^{n_I,k-1}$ and $\beta^{n_I,k-1}$ are numerical parameters defined in Fig. B.1.

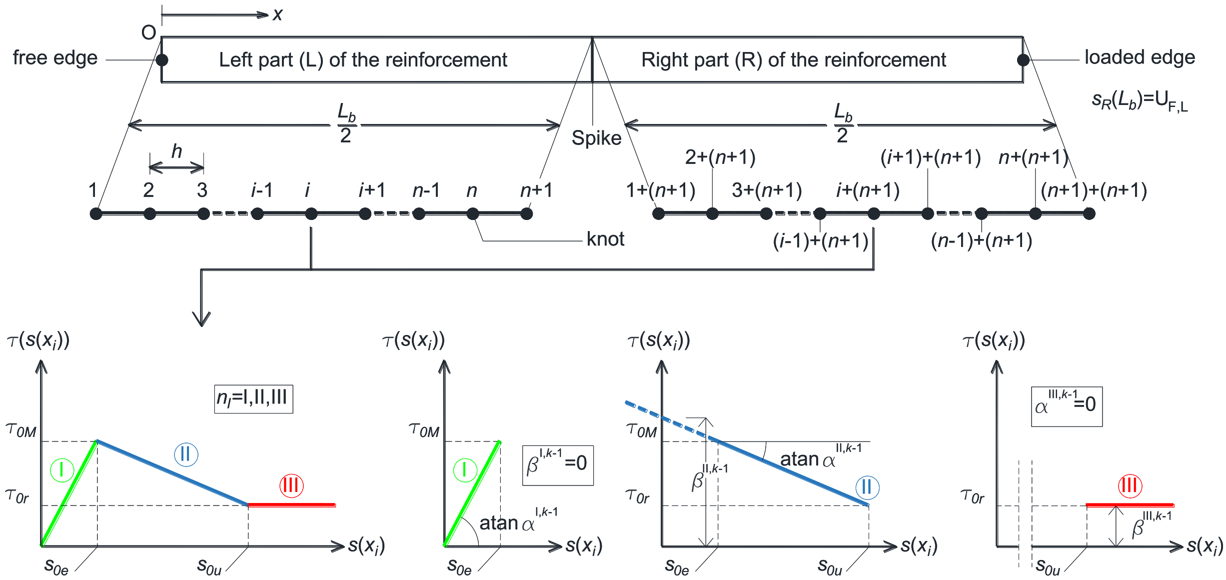

Fig. B.1. Space partitioning adopted in the BVP and meaning of $\alpha^{n_I,k-1}$ and $\beta^{n_I,k-1}$ parameters.

Eq. (B2) is a set of two equations where independent variables are $y_1^{i+1}, y_2^{i+1}, y_1^i$ and y_2^i. They are imposed for each spatial partition belonging to the Left (L) and Right part (L), see Fig. B.1, so that in total $4n$ equations can be written. On the other hand, the total number of variables is $2(2n+2) = 4n + 4$. Consequently, four additional equations are needed to deduce variables y_1^i and y_2^i by solving a standard system of linear equations. Two of them are imposed at the free and loaded edges as follows:

$$\begin{aligned} &y_2^1 = 0 \\ &y_1^{2n+2} = U_{F,L} \end{aligned} \tag{B3}$$

In correspondence with the spike, two other equations must be written to ensure continuity of the fiber stress field and the slip gap observed between the Left and Right parts and induced by the spike:

$$\begin{aligned} y_2^{n+2} &= y_2^{n+1} \\ y_1^{n+2} &= y_1^{n+1} + \frac{y_2^{n+1}}{K_s} E_F t_F \end{aligned} \tag{B4}$$

Eqs. (B2), (B3), and (B4), suitably assembled, represent a system of $4n+4$ linear equations that allows the determination of $\boldsymbol{y}$ vector (length equal to $4n + 4$) at each time step.

For illustrative purposes, in Fig. B.2 the numerical global behavior of the CAI WAS sample (force F_L vs displacement $U_{F,L}$ applied at the free edge) obtained using Euler forward finite differences is compared with that provided by the model proposed in this paper (IVP solved with a 4$^{\text{th}}$ order Runge-Kutta scheme). For the Euler forward finite difference scheme, two spatial partitioning sizes h -respectively equal to $L_b/1000$, dashed-dotted line, and $L_b/10000$, continuous line) are adopted. As expected, the response is identical almost everywhere, with the exception made in the snap-back regions, which cannot be reproduced when a monotonically increasing slip is applied at the loaded edge. Furthermore, finite differences are affected by visible numerical instability immediately before and after the snap-back triggering, which is progressively alleviated -but still present- when the spatial partitioning size is reduced. Such an outcome was largely expected because there are many sources of error introduced in the standard BVP kernel adopted, the most important being the following: (i) spatial derivatives are written with a forward scheme, and (ii) mechanical properties of the interface and normal stress at the interface are those obtained in the previous time step (k-1).

Whilst for the first matter a more sophisticated derivative scheme is recommended (for instance the adoption of central differences), the latter -which does not occur in the IVP- is intrinsically unavoidable and requires either considerable refinements of the time steps or the adoption of iterative or adaptive procedures in the application of $U_{F,L}$. It has been proved by some of the authors of this paper in a less demanding debonding problem [58] that the error may be dropped down when a finite difference algorithm that implements the 3-stage Lobatto IIIa formula is adopted, but the numerical efficiency still remains far lower than that exhibited by the IVP scheme. Indeed, for the example at hand, IVP required less than one minute to run in a standard laptop equipped with 32Gb RAM and a 12th Gen Intel(R) Core(TM) i7-1255U at 1.70 GHz. On the contrary, the same BVP solved using finite differences took respectively 4 hours and 53 minutes assuming $h = L_b/10000$ and about 6 minutes for $h = L_b/1000$.

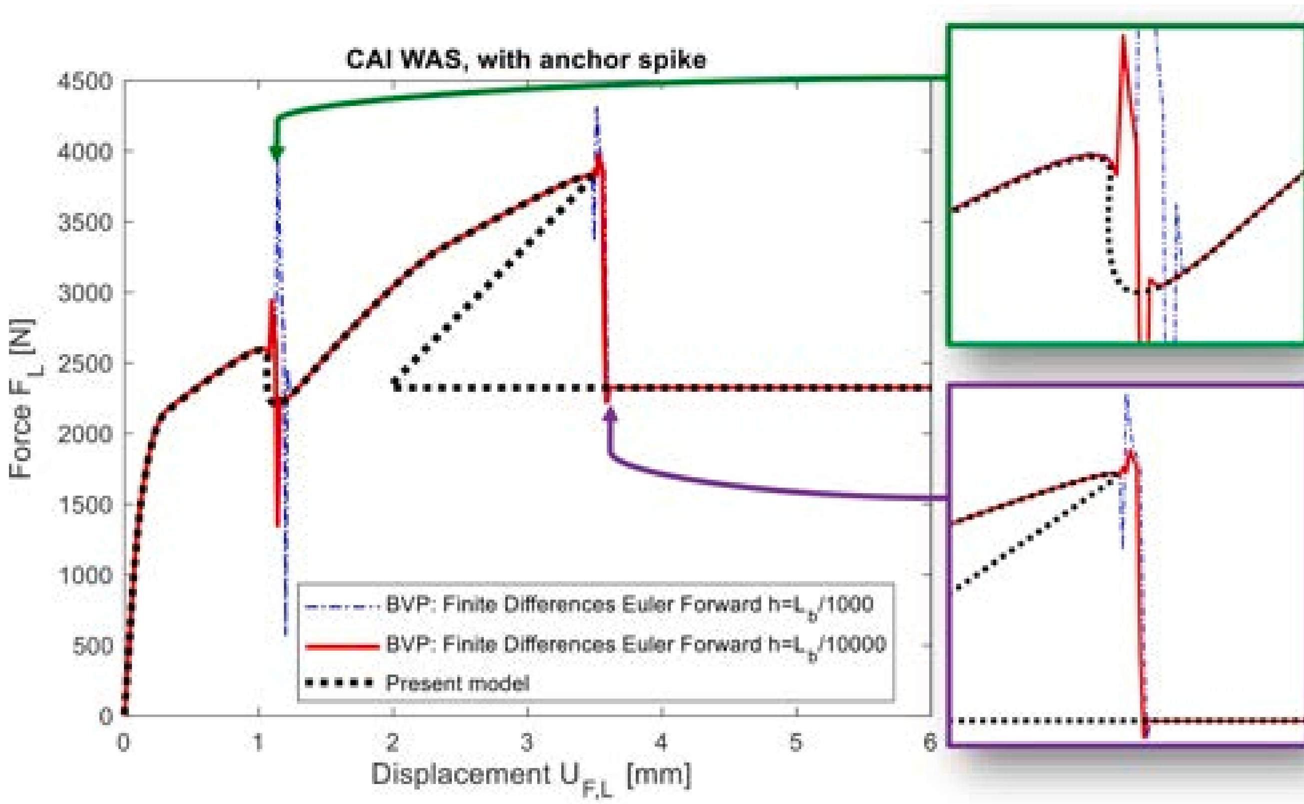

Fig. B.2. CAI WAS, curved sample at high curvature with anchor spike. Comparison between numerical global behavior obtained with the present model (dotted black line) and that provided by an Euler forward finite difference method (BVP) with two spatially different discretization lengths (blue dashed-dotted curve: $h=L_b/1000$; red continuous curve: $h=L_b/10000$).

Appendix C. Spike exhibiting a non-linear behavior

The model proposed is phenomenological, so it may become interesting to evaluate the opportunity to model the spike as a non-linear spring. Two distinct cases are possible, depending on whether the spike exhibits hardening or softening.

Let us assume that the spike is characterized respectively by bilinear and trilinear behavior in the first and second case, see Fig. C.1. All the additional parameters necessary to characterize the spring are explicitly indicated in Fig. C.1.

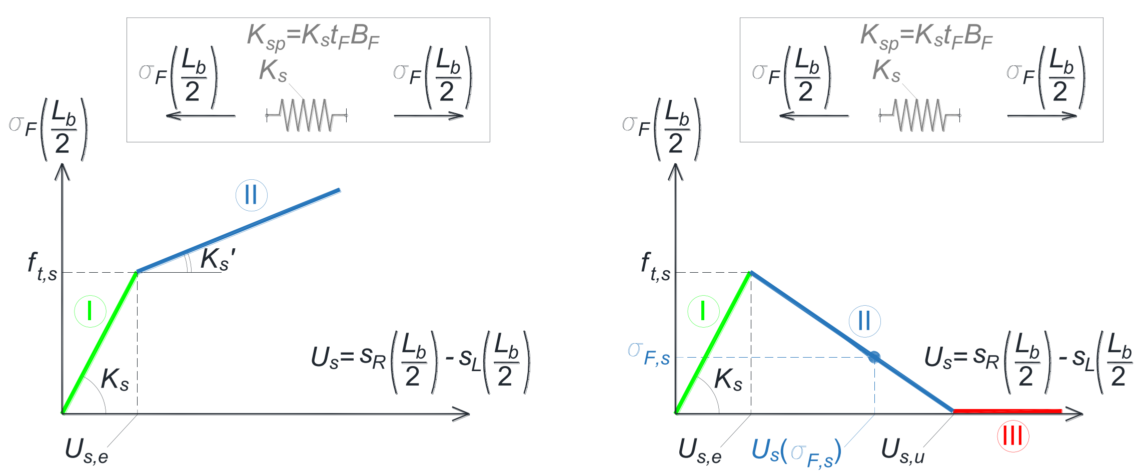

Fig. C.1. Schematic representation of the constitutive behavior of the spike. Bilinear with hardening (left) and trilinear with softening (right).

In case of hardening, there are no relevant methodological differences with respect to the case when the spring is assumed elastic. The only modification stems in the evaluation of $s_R\left(\frac{L_b}{2}\right)$ in Eq. (10), which for a spike exhibiting linear hardening modifies as follows:

$$
\begin{aligned}
& s_R\left(\frac{L_b}{2}\right) = s_L\left(\frac{L_b}{2}\right) + \frac{s_L'\left(\frac{L_b}{2}\right)E_F}{K_s} && s_L'\left(\frac{L_b}{2}\right)E_F \le f_{t,s} \\
& s_R\left(\frac{L_b}{2}\right) = s_L\left(\frac{L_b}{2}\right) + U_{s,e} + \frac{s_L'\left(\frac{L_b}{2}\right)E_F - f_{t,s}}{K_s'} && s_L'\left(\frac{L_b}{2}\right)E_F > f_{t,s}
\end{aligned}
\tag{C1}
$$

Where $U_{s,e}$ is the elongation of the spring representing the spike at the elastic limit and $f_{t,s}$ is the corresponding stress.

When the constitutive behavior of the spike is characterized by a trilinear law with softening, characterized by a peak stress equal to $f_{t,s}$, as soon as the reinforcement layer reaches $f_{t,s}$ in correspondence of spike location, i.e. $s_L'\left(\frac{L_b}{2}\right)E_F = f_{t,s}$, the left part is enforced to undergo an unloading phase.

Consequently, since the family of models whose the present one belongs is intrinsically holonomic (total displacements/slips are applied, regardless of the numerical method used), the response makes physical sense only if the left part is assumed in the elastic range when $f_{t,s}$ is reached, otherwise incremental models and loading/unloading laws are needed.

Assuming that the spike is in the softening stage (phase II of Fig. C.1, right) and that at spike location the tensile stress in the reinforcement is equal to $\sigma_{F,s}$, then combining Eqs. (A1) and (A2), the slip applied at the free edge and the slip of the left part of the reinforcement in correspondence of the spike are the following:

$$
\begin{aligned}
& \bar{s}_{l0} = \frac{2}{E_F\alpha}\frac{\sigma_{F,s}}{-e^{-\alpha\frac{L_b}{2}} + e^{\alpha\frac{L_b}{2}}} \\
& s_L\left(\frac{L_b}{2}\right) = \frac{\sigma_{F,s}}{E_F\alpha}\frac{e^{-\alpha\frac{L_b}{2}} + e^{\alpha\frac{L_b}{2}}}{-e^{-\alpha\frac{L_b}{2}} + e^{\alpha\frac{L_b}{2}}}
\end{aligned}
\tag{C2}
$$

The elongation of the spike when the tensile stress is $\sigma_{F,s}$ -labeled here as $U_s(\sigma_{F,s})$- can be calculated directly from the constitutive law, see Fig. C.1, as follows:

$$
U_s(\sigma_{F,s}) = -(U_{s,u} - U_{s,e})\frac{\sigma_{F,s} - f_{t,s}}{\sigma_{F,s}} + U_{s,e} \tag{C3}
$$

where $U_{s,u}$ is the ultimate elongation of the spring representing the spike and $U_{s,e}$ is the elongation at the elastic limit.

With the relations provided in Eqs. (C2) and (C3), the slip $s_R\left(\frac{L_b}{2}\right)$ is calculated as follows:

$$
s_R\left(\frac{L_b}{2}\right) = -(U_{s,u} - U_{s,e})\frac{\sigma_{F,s} - f_{t,s}}{\sigma_{F,s}} + U_{s,e} + \frac{\sigma_{F,s}}{E_F\alpha}\frac{e^{-\alpha\frac{L_b}{2}} + e^{\alpha\frac{L_b}{2}}}{-e^{-\alpha\frac{L_b}{2}} + e^{\alpha\frac{L_b}{2}}} \tag{C4}
$$

At the end of stage II, the spring representing the spike is unable to transmit tensile stresses, the left part of the reinforcement is inactive, and the debonding problem for the right part is again solved by means of the RK4 kernel of Eqs. (13)-(15):

$$
\frac{L_b}{2} < x \le L_b \begin{cases} \dfrac{ds_R'}{dx} = \dfrac{\tau(s_R)}{E_F t_F} \\ \dfrac{ds_R}{dx} = s_R' \end{cases} \text{with initial conditions} \begin{cases} s_R\left(\dfrac{L_b}{2}\right) = \bar{s}_R \ge U_{s,u} \\ s_R'\left(\dfrac{L_b}{2}\right) = 0 \end{cases} \tag{C5}
$$

Where $\bar{s}_R$ is the slip applied to the right part in correspondence of the spike.

For illustrative purposes, the flat case is reconsidered here with the same mechanical and geometrical properties previously established, but here considering that the spike anchor behaves non-linearly. A sensitivity analysis is carried out, both hypothesizing hardening and softening behaviors, according to the data provided in Table C.1. Three different models for the hardening and softening cases are investigated, changing respectively the values assumed for K_s' in the former case and those of $U_{s,u}$ in the latter.

Results obtained in terms of global force-displacement curves are depicted in Fig. C.2. As it is possible to notice, when the spike's spring exhibits hardening, the ultimate displacement increases. As expected, the resultant behavior is qualitatively similar to that observed in Appendix A (see Fig. A.3-a), where the spike is assumed elastic, but with stiffness progressively reduced. Unlike the Appendix A case, however, the intermediate drop in load carrying capacity remains essentially unaltered. Furthermore, it is difficult to tune the additional parameters necessary to fully define the spike constitutive behavior (i.e. $\sigma_{F,s}$ and K_s'), differently from what done for K_s, where a straightforward estimation is possible, as thoroughly discussed in Appendix A.

Conversely, when the constitutive behavior of the spike is assumed trilinear with softening, the resultant global response visibly deviates from experimental evidence, see Fig. C.2-c and -d. Both sets of results obtained were largely foreseeable. Especially for the softening case, it is worth mentioning that the phenomenological approach proposed is based on modelling the reinforcement system with central spike where non-linearities are disposed in series (left part, spike and right part). When the spike reaches complete damage, there is no possibility to transfer loads from the right to the left, with the consequent divergence from experimental data.

On the basis of the above results, it is possible to observe that, although the proposed non-linear formulations allow for a more refined representation of the spike behavior, the comparison with experimental results highlights that these models do not necessarily improve the predictive capability of the approach. In particular, the introduction of softening in the spike response leads to an earlier reduction of the load transfer capacity, resulting in a global response that departs from the experimentally observed plateau-like behavior.

Furthermore, the identification of the additional parameters required by the non-linear spike laws is affected by significant uncertainty, due to the complex and highly variable local damage mechanisms governing spike activation. As a result, the adoption of more complex constitutive laws does not provide a clear advantage in terms of robustness and predictability.

For these reasons, the linear elastic representation of the spike is retained in the main formulation as a pragmatic and sufficiently accurate approximation.

Table C.1
Mechanical properties adopted for the spike, assumed exhibiting either hardening or softening ($f_{t,s}$=1000 MPa, $K_s = 4960\frac{N}{mm^3}$).

Hardening		Softening	
Model SH1	$K_s' = 0.7K_s$	Model SS1	$U_{s,u} = 4U_{s,e}$
Model SH2	$K_s' = 0.5K_s$	Model SS2	$U_{s,u} = 8U_{s,e}$
Model SH3	$K_s' = 0.3K_s$	Model SS3	$U_{s,u} = 12U_{s,e}$

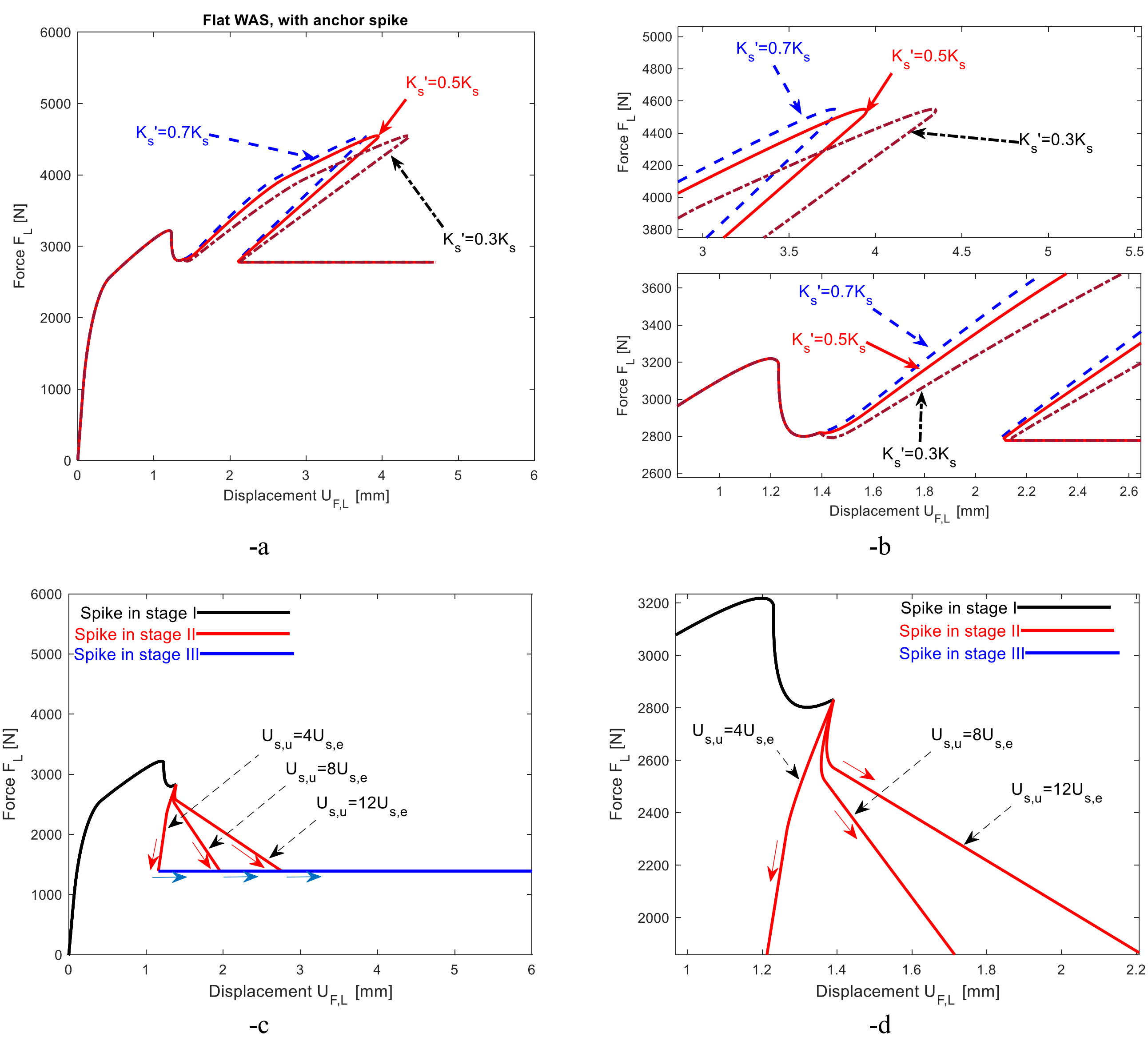

Fig. C.2. Flat case, global force-displacement curves provided by the model assuming for the spike (-a & -b) a bilinear hardening (Models SH1, SH2 and SH3) and (-c & -d) a trilinear softening (Models SS1, SS2 and SS3).

References

[1] Giordano E, Bertolesi E, Clementi F, Buitrago M, Adam JM, Ivorra S. Unreinforced and TRM-reinforced masonry building subjected to pseudodynamic excitations: numerical and experimental insights. J Eng Mech 2021;147(12):04021107.

[2] Meriggi P, Nerilli F, Fares S, Fugger R, Marfia S, Sacco E, et al. Shear mechanisms in fabric-reinforced cementitious matrix overlays: experimental and numerical investigation. J Compos Constr 2023;27(4):04023032.

[3] Plassiard JP, Alachek I, Plé O. Damage-based finite-element modelling of in-plane loaded masonry walls repaired with FRCM. Comput Struct 2021;254:106481.

[4] Giordano E, Masciotta MG, Clementi F, Ghiassi B. Numerical prediction of the mechanical behavior of TRM composites and TRM-strengthened masonry panels. Constr Build Mater 2023;397:132376.

[5] Pourfalah S, Cotsovos DM, Suryanto B. Modelling the out-of-plane behaviour of masonry walls retrofitted with engineered cementitious composites. Comput Struct 2018;201:58–79.

[6] Zampieri P, Simoncello N, Gonzalez-Libreros J, Pellegrino C. Evaluation of the vertical load capacity of masonry arch bridges strengthened with FRCM or SFRM by limit analysis. Eng Struct 2020;225:111135.

[7] Bertolesi E, Buitrago M, Giordano E, Calderón PA, Moragues JJ, Clementi F, et al. Effectiveness of textile reinforced mortar (TRM) materials in preventing seismic-induced damage in a U-shaped masonry structure submitted to pseudo-dynamic excitations. Constr Build Mater 2020;248:118532.

[8] De Santis S, de Felice G, Di Noia G, Meriggi P, Volpe M. Shake table tests on a masonry structure retrofitted with composite reinforced mortar. Key Eng Mater 2019;817:342–9. https://doi.org/10.4028/www.scientific.net/KEM.817.342.

[9] Fares S, Meriggi P, De Santis S, de Felice G. Experimental investigation on the tensile and bond durability of galvanized steel reinforced grout. Buildings 2025;15 (17):3020.

[10] Misseri G, Rovero L, Stipo G, Barducci S, Alecci V, De Stefano M. Experimental and analytical investigations on sustainable and innovative strengthening systems for masonry arches. Compos Struct 2019;210:526–37.

[11] Alecci V, Focacci F, Rovero L, Stipo G, De Stefano M. Intrados strengthening of brick masonry arches with different FRCM composites: experimental and analytical investigations. Compos Struct 2017;176:898–909.

[12] D'Ambrisi A, Feo L, Focacci F. Experimental analysis on bond between PBO FRCM strengthening materials and concrete. Compos B Eng 2013;44(1):524–32.

[13] De Santis S, Ceroni F, de Felice G, Fagone M, Ghiassi B, Kwiecien A, et al. Round robin test on tensile and bond behaviour of steel reinforced grout systems. Compos B Eng 2017;127:100–20.

[14] Ombres L, Mancuso N, Mazzuca S, Verre S. Bond between carbon fabric-reinforced cementitious matrix and masonry substrate. J Mater Civ Eng 2019;31:04018356.

[15] Bertolesi E, Fagone M, Rotunno T, Grande E, Milani G. Experimental characterization of the textile-to-mortar bond through distributed optical sensors. Constr Build Mater 2022;326:126640.

[16] D'Ambrisi A, Feo L, Focacci F. Experimental and analytical investigation on bond between Carbon-FRCM materials and masonry. Compos B Eng 2013;46:15–20.

[17] Razavizadeh A, Ghiassi B, Oliveira DV. Bond behavior of SRG-strengthened masonry units: testing and numerical modeling. Constr Build Mater 2014;64: 387–97.

[18] Ghiassi B, Xavier J, Oliveira DV, Lourenço PB. Application of digital image correlation in investigating the bond between FRP and masonry. Compos Struct 2013;106:340–9.

[19] Grande E, Imbimbo M, Sacco E. Investigation on the bond behavior of clay bricks reinforced with SRP and SRG strengthening systems. Mater Struct 2015;48(11): 3755–70.

[20] Ramaglia G, Mecca I, Angrisano M, Santagata R, Olivieri C. An optimization-based framework for the structural strengthening of masonry buildings. Int J Space Struct 2025;40(2–3):170–9.

[21] Nerilli F, Marfia S, Sacco E. Nonlocal damage and interface modeling approach for the micro-scale analysis of FRCM. Comput Struct 2021;254:106582.

[22] Milani G, Grande E. Simple bisection procedure in quickly convergent explicit ODE solver to numerically analyze FRCM strengthening systems. Compos B Eng 2020; 199:108322.

[23] Milani G. Semi-analytical mechanical model for FRCM-to-substrate shear bond tests. Compos B Eng 2023;266:110983.

[24] Minafò G, Di Leto M, Camarda G, La Mendola L. A GA-based model updating procedure for the numerical simulation of FRCM-to-masonry bond. Eng Struct 2024;303:117512.

[25] Oddo MC, Minafò G, Di Leto M, La Mendola L. Numerical modelling of the constitutive behaviour of FRCM composites through the use of truss elements. Materials 2023;16(3):1011.

[26] Minafò G, Oddo MC, La Mendola L. Formulation of a truss element for modelling the tensile response of FRCM strips. Constr Build Mater 2022;315:125576.

[27] Calabrese AS, Colombi P, D'Antino T. Analytical solution of the bond behavior of FRCM composites using a rigid-softening cohesive material law. Compos B Eng 2019;174:1–10.

[28] Pingaro N, Calabrese AS, Milani G, Poggi C. Debonding sawtooth analytical model and FE implementation with in-house experimental validation for SRG-strengthened joints subjected to direct shear. Compos Struct 2023;319:117113.

[29] Carozzi FG, Colombi P, Fava G, Poggi C. A cohesive interface crack model for the matrix–textile debonding in FRCM composites. Compos Struct 2016;143:230–41.

[30] Rotunno T, Fagone M, Grande E, Milani G. FRCM-to-masonry bonding behaviour in the case of curved surfaces: experimental investigation. Compos Struct 2023;313: 116913.

[31] Malena M, de Felice G. Debonding of composites on a curved masonry substrate: Experimental results and analytical formulation. Compos Struct 2014;112: 194–206.

[32] Bertolesi E, Torres B, Adam JM, Calderón PA, Moragues JJ. Effectiveness of Textile Reinforced Mortar (TRM) materials for the repair of full-scale timbrel masonry cross vaults. Eng Struct 2020;220:110978.

[33] Castellano A, Fraddosio A, Oliveira DV, Piccioni MD, Ricci E, Sacco E. An effective numerical modelling strategy for FRCM strengthened curved masonry structures. Eng Struct 2023;274:115116.

[34] Malena M. Closed-form solution to the debonding of mortar based composites on curved substrates. Compos B Eng 2018;139:249–58.

[35] Scacco J, Milani G, Lourenço PB. A micro-modeling approach for the prediction of TRM bond performance on curved masonry substrates. Compos Struct 2021;256: 113065.

[36] Pingaro N, Milani G. Non-linear 1D 16-DOF finite element for Fiber Reinforced Cementitious Matrix (FRCM) strengthening systems. Comput Struct 2024;300: 107422.

[37] Grande E, Fagone M, Rotunno T, Milani G. Modeling of shear-lap tests of flat and curved masonry specimens strengthened by FRCM. Structures 2023;52:437–48.

[38] Milani G, Grande E, Rotunno T, Fagone M. Semi-analytical approach for curved masonry pillars reinforced with FRCM. Compos Struct 2024;337:118037.

[39] Yuan Y, Milani G. Simple double shooting approach with bisection for FRCM reinforced curved masonry prisms subjected to shear. Compos Struct 2024;345: 118363.

[40] Bertolesi E, Grande E, Fagone M, Milani G, Rotunno T. Mechanical model based on a BVP for FRPs applied on flat and curved masonry pillars with anchor spikes. Compos Struct 2021;273:114251.

[41] Caggegi C, Pensee V, Fagone M, Cuomo M, Chevalier L. Experimental global analysis of the efficiency of carbon fiber anchors applied over CFRP strengthened bricks. Constr Build Mater 2014;53:203–12.

[42] Rotunno T, Fagone M, Bertolesi E, Grande E, Milani G. Curved masonry pillars reinforced with anchored CFRP sheets: an experimental analysis. Compos B Eng 2019;174:#107008.

[43] Zampieri P, Santinon D, Pellegrino C, Iodice F, Vecchi A. Effect of spike anchors in the bond behavior of FRCM systems applied onto curved masonry substrates. J Compos Constr 2023;27(6):04023061.

[44] Pingaro N, Fagone M, Rotunno T, Grande E, Milani G. Experimental study on the influence of spike anchors on the bond of FRCM systems applied to curved masonry specimens. Constr Build Mater 2026;513:#145338.

[45] Zampieri P, Santinon D, Pellegrino C, Iodice F, Vecchi A. Influence of spike anchors in the bond behaviour of FRCM systems applied on concave masonry substrates. Procedia Struct Integrity 2024;62:446–53.

[46] Zampieri P, Santinon D, Niero L, Pellegrino C, Gonzalez-Libreros J, Sas G. Effect of the spike anchors on the failure mode of a FRCM system applied to a curved masonry substrate. Structures 2025;79:109522.

[47] Cornetti P, Carpinteri A. Modelling the FRP-concrete delamination by means of an exponential softening law. Eng Struct 2011;33(6):1988–2001.

[48] Xu XF. Multiscale theory of composites and random media. CRC Press, Taylor & Francis Group, 1st Edition, 2020. ISBN 9780367657024.

[49] Joseph PG. Dynamical systems-based soil mechanics. CRC Press, Taylor & Francis Group, 1st Edition, 2017. ISBN 9781138723221.

[50] Portides D. Seeking representations of phenomena: phenomenological models. Stud Hist Philos Sci Part A 2011;42(2):334–41.

[51] Siegel G, Craver CF. Phenomenological laws and mechanistic explanations. Philos Sci 2024;91(1):132–50.

[52] Mirzaei AM, Corrado M, Sapora A, Cornetti P. Analytical modeling of debonding mechanism for long and short bond lengths in direct shear tests accounting for residual strength. Materials 2021;14:6690.

[53] Caggiano A, Martinelli E, Faella C. A fully-analytical approach for modelling the response of FRP plates bonded to a brittle substrate. Int J Solids Struct 2012;49: 2291–300.

[54] Cornetti P, Corrado M, De Lorenzis L, Carpinteri A. An analytical cohesive crack modeling approach to the edge debonding failure of FRP-plated beams. Int J Solids Struct 2015;53:92–106.

[55] Nelson LA, Al-Allaf M, Weekes L. Analytical modelling of bond-slip failure between epoxy bonded FRP and concrete substrate. Compos Struct 2020;251:112596.

[56] Zou X, D'Antino T, Sneed LH. Analytical study of the bond behavior of fiber reinforced cementitious matrix (FRCM)-substrate joints based on a two-stage nonlinear cohesive material law. Compos Struct 2023;304:116457.

[57] Zhu M, Ueda T, Zhu J. Generalized evaluation of bond behavior of the externally bonded FRP reinforcement to concrete. J Compos Constr 2020;24(6):04020066.

[58] Milani G, Fagone M, Rotunno T, Grande E, Bertolesi E. Development of an interface numerical model for C-FRPs applied on flat and curved masonry pillars. Compos Struct 2020;241:112074.